ARL-TR-8837 ● Oct 2019

Investigation of Bistatic Radar Imaging for Counter-Explosive Hazard Applications

by Traian Dogaru

NOTICES

Disclaimers

ARL-TR-8837 ● OCT 2019

Investigation of Bistatic Radar Imaging for Counter-Explosive Hazard Applications

Traian Dogaru
Sensors and Electron Devices Directorate, CCDC Army Research Laboratory

REPORT DOCUMENTATION PAGE			*Form Approved OMB No. 0704-0188*

1. REPORT DATE *(DD-MM-YYYY)*	2. REPORT TYPE	3. DATES COVERED (From - To)
October 2019	Technical Report	March 2017–June 2018

4. TITLE AND SUBTITLE	5a. CONTRACT NUMBER
Investigation of Bistatic Radar Imaging for Counter-Explosive Hazard Applications	5b. GRANT NUMBER
	5c. PROGRAM ELEMENT NUMBER
6. AUTHOR(S)	**5d. PROJECT NUMBER**
Traian Dogaru	5e. TASK NUMBER
	5f. WORK UNIT NUMBER
7. PERFORMING ORGANIZATION NAME(S) AND ADDRESS(ES)	**8. PERFORMING ORGANIZATION REPORT NUMBER**
CCDC Army Research Laboratory ATTN: FCDD- RLS-RU 2800 Powder Mill Road, Adelphi, MD 20783-1138	ARL-TR-8837
9. SPONSORING/MONITORING AGENCY NAME(S) AND ADDRESS(ES)	**10. SPONSOR/MONITOR'S ACRONYM(S)**
US Army Combat Capabilities Development Command, Command, Control, Computers, Communications, Cyber, Intelligence, Surveillance and Reconnaissance, Night Vision Electronics and Sensors Directorate Aberdeen Proving Ground, MD	CCDC C5ISR NVESD **11. SPONSOR/MONITOR'S REPORT NUMBER(S)**

12. DISTRIBUTION/AVAILABILITY STATEMENT

Approved for public release; distribution is unlimited.

13. SUPPLEMENTARY NOTES

ORCID ID: Traian Dogaru, 0000-0002-1091-4928

14. ABSTRACT

This report is an investigation into whether active, coherent bistatic radar systems are a viable solution for imaging and detection of counter-explosive hazards (CEHs). The study is based on computer models of the radar signatures of targets typical for this application, such as shallow-buried landmines. These models allow us to evaluate the bistatic target radar cross section as well as the target-to-clutter ratio, in the presence of distributed terrain clutter, for various sensing geometries and polarizations. This is followed by an analysis of the images obtained by the bistatic radar system, both in the near- and far-field regions. This analysis emphasizes the significant loss of image resolution at large bistatic angles as well as the difficulty to separate the target response from the specular ground bounce. Since better performance can be readily achieved with traditional quasi-monostatic radar systems, we conclude that bistatic radar imaging at large bistatic angles is not a suitable solution for CEH applications.

15. SUBJECT TERMS

bistatic radar, radar imaging, counter-explosive hazard, point spread function, radar modeling

16. SECURITY CLASSIFICATION OF:			17. LIMITATION OF ABSTRACT	18. NUMBER OF PAGES	19a. NAME OF RESPONSIBLE PERSON
					Traian Dogaru
a. REPORT	**b. ABSTRACT**	**c. THIS PAGE**			**19b. TELEPHONE NUMBER (Include area code)**
Unclassified	Unclassified	Unclassified	UU	76	(301) 394-1482

Standard Form 298 (Rev. 8/98)
Prescribed by ANSI Std. Z39.18

Contents

List of Figures

List of Tables

Acknowledgments

I would like to thank Aaron LaPointe, William Clark, Brian Burns, Ton Tuan, and David Wong from the US Army Combat Capabilities Development Command, Command, Control, Computers, Communications, Cyber, Intelligence, Surveillance and Reconnaissance, Night Vision Electronics and Sensors Directorate, who funded and took interest in this work.

1. Introduction

Detection of explosive hazards, including landmines, unexploded ordnance, and improvised explosive devices is an important military application of radar technology. Both the US Army Combat Capabilities Development Command (CCDC), Command, Control, Communications, Computers, Combat Systems, Intelligence, Surveillance, and Reconnaissance Night Vision and Electronic Sensors Directorate, and the CCDC Army Research Laboratory (ARL) have been at the forefront of this technology for more than 20 years, conducting various Department of Defense counter-explosive hazard (CEH) programs. Several collaborative efforts between the two agencies have produced significant advances in this area, exemplified by the Alaric,[1] Synchronous Impulse Reconstruction (SIRE),[2] and Spectrally Agile Frequency-Incrementing Reconfigurable (SAFIRE)[3] forward-looking radar systems.

More recently, Army researchers started to investigate whether bistatic radar configurations can offer any advantages in CEH applications as compared with the conventional quasi-monostatic, forward-looking synthetic aperture radar (FLSAR). Strictly speaking, all the existing FLSAR systems operate in bistatic geometries with very small bistatic angles between transmitter (Tx), target, and receiver (Rx). However, the new investigation proposes geometries involving large bistatic angles, from 0° to 180°, by removing the restriction of installing the Tx and Rx antennas on the same physical platform.

This radical departure from conventional radar imaging geometries presents new phenomenological challenges which, to our knowledge, have not been widely documented in the open literature. General material available in texts dedicated to bistatic radar technology[4–6] emphasize the changes in target signature and radar resolution as a function of the bistatic geometry. However, we were not able to find a systematic study of these issues in the context of radar imaging and their impact on radar detection performance. The current investigation is an attempt at filling this gap by exploring the phenomenology and potential performance of bistatic radar imaging via computer models.

This report is organized as follows. Section 2 formulates the problem under investigation and describes the methods employed in the numerical analysis. In Section 3, we perform calculations of the target and clutter signatures for bistatic radar geometries and find the optimum configurations in terms of target-to-clutter ratio (TCR). Section 4 goes through an analysis of near-field bistatic radar images, with numerical examples of both the point spread function (PSF) and realistic target simulations. The *k*-space analysis of far-field bistatic radar images in Section 5 provides a rigorous explanation of resolution as a function of sensing geometry. Section 6 presents the simulation of an FLSAR system that emphasizes the differences in imaging performance between quasi-monostatic and bistatic configurations. We draw conclusions in Section 7.

2. Problem Statement and Methodology

This report's objective is to investigate whether an active, coherent bistatic imaging radar system can provide improved performance compared with a conventional monostatic radar in CEH applications. The sensing geometry relevant to this application is shown in Fig. 1. In most of the models considered throughout this work, the position of the radar Tx is kept fixed, while the Rx is configured either as a fixed antenna array or a moving element forming a synthetic aperture. The target is a shallow-buried underground object, with the rough terrain surface providing distributed clutter to the scene. The image is created in the ground plane, without attempting to infer information on the target depth. Note that this sensing geometry is a hypothetical model that, to our knowledge, does not currently have a practical implementation counterpart.

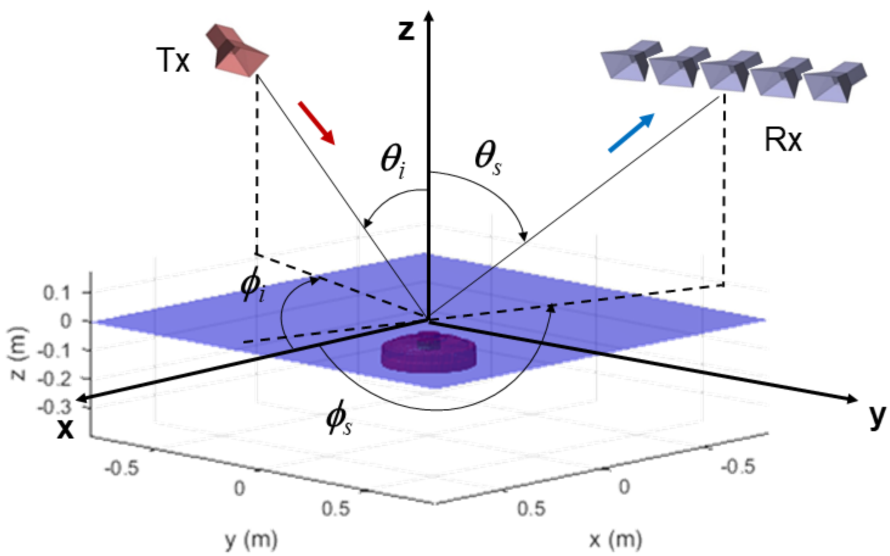

Fig. 1 Geometry of a generic bistatic imaging radar system equipped with one Tx and an Rx antenna array

Before we discuss the potential advantages and disadvantages of bistatic radar systems, we introduce some of the terminology specific to this sensing modality. Thus, Fig. 2 illustrates the possible propagation paths between Tx and Rx: direct, specular (reflected from the ground surface), and scattered (reflected by the target). Figure 2c defines the bistatic angle β, as well as the bisector of this angle. The angle

δ is measured between the bistatic angle bisector and its projection onto the ground plane.

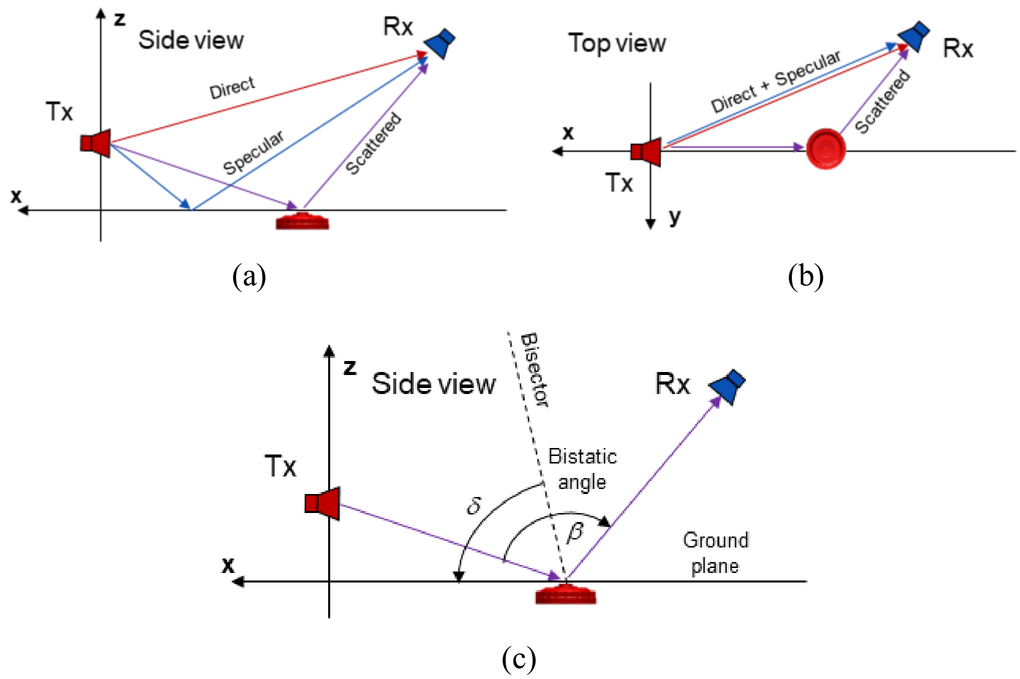

Fig. 2 Description of the radar wave propagation paths between the Tx, target and Rx, showing a) side view, b) top view, and c) side view defining the bistatic angle and its bisector

In Fig. 3 we define the angles and directions of propagation. Thus, the pair of incidence angles (ϕ_i, θ_i) represents the direction of the Tx location, while the pair of scattering angles (ϕ_s, θ_s) represents the direction of the Rx location, both starting from the origin. The propagation directions of the incident and scattered plane waves are given by the following unit vectors:

$$\hat{\mathbf{k}}_i = \begin{bmatrix} -\cos\phi_i \sin\theta_i \\ -\sin\phi_i \sin\theta_i \\ -\cos\theta_i \end{bmatrix} \qquad \hat{\mathbf{k}}_s = \begin{bmatrix} \cos\phi_s \sin\theta_s \\ \sin\phi_s \sin\theta_s \\ \cos\theta_s \end{bmatrix}. \tag{1}$$

The ϕ angles are allowed to vary around the clock (from 0° to 360°), whereas the θ angles are limited to the interval between 0° and 90°. The backscattering configuration (encountered in monostatic radar) involves the following relations: $\phi_s = \phi_i$ and $\theta_s = \theta_i$. Another important bistatic configuration for radar geometries involving a ground plane is specular scattering, which occurs when $\phi_s - \phi_i = 180°$ and $\theta_s = \theta_i$. Note that this configuration corresponds to what most texts call "forward scattering" for free-space propagation. When the Tx, the target, and the Rx are all in the same vertical plane (meaning $\phi_s - \phi_i = 0°$ or 180°), we talk about "in-plane" scattering (Fig. 4a). When $\phi_s - \phi_i$ takes any other values, the scattering geometry is called "out-of-plane" (Fig. 4b).

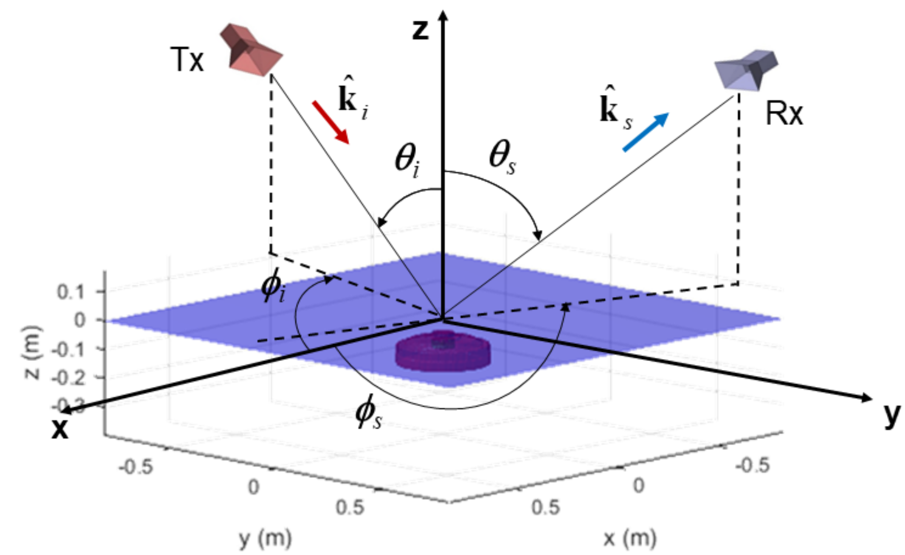

Fig. 3 Geometry of a generic bistatic radar system showing the propagation directions of the incident and scattered waves, as well as the corresponding propagation angles

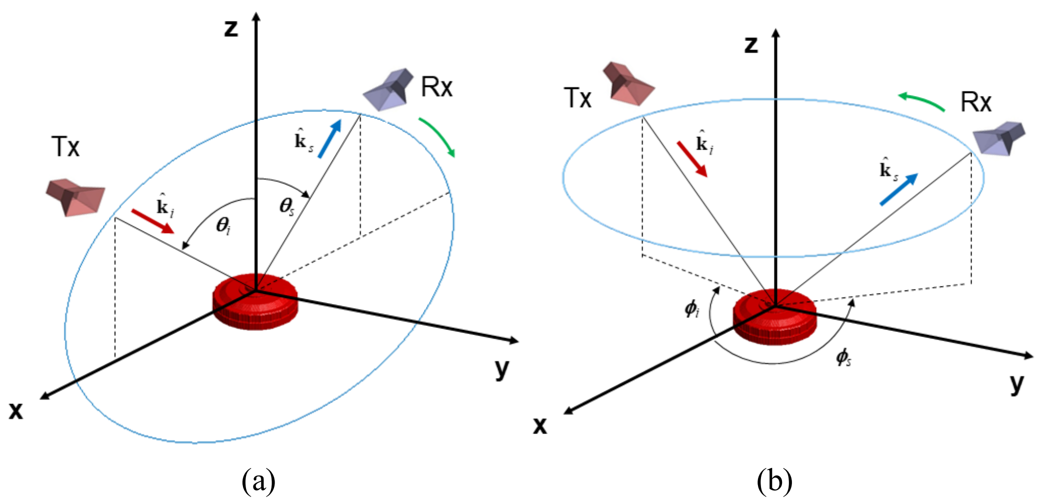

Fig. 4 Schematic diagram of two angle sweeping configurations, showing a) in-plane scattering and b) out-of-plane scattering

To understand the evaluation criteria of radar system performance in detecting these low-signature, concealed, and stationary targets, it helps to remind the reasons why high-resolution radar imaging is a viable solution for these sensing scenarios:

- It concentrates the entire target return energy in a small volume/area of the image.
- It separates the target from discrete clutter objects (bushes, rocks, etc.).
- It enhances the TCR for distributed clutter (e.g., rough terrain) by reducing the resolution cell size.
- It could help in target classification process if the target extends over multiple resolution cells.

A review of these requirements reveals that achieving good image resolution is paramount in fulfilling all four of them. For CEH radar systems operating at low microwave frequencies (0.3–3.0 GHz), this is typically obtained by employing ultra-wideband (UWB) waveforms and wide angle coherent integration (as in synthetic aperture radar [SAR] systems). At the same time, large TCR is another desirable performance metric. Therefore, this study focuses on evaluating the image resolution and the TCR as indicators of radar detection performance.

Bistatic radar systems have the potential to improve radar detection by providing large target signatures at certain look angles.[4] Given the fact that the imaging procedure can integrate a wide range of aspect angles, these may well include the ones offering the maximum target response. In Section 3 we search for these angles based on computer models of target and clutter radar cross section (RCS).

Nevertheless, the bistatic radar systems present some major drawbacks as well. Thus, the time and phase synchronization between Tx and Rx channels is a serious issue that significantly complicates the system design and does not have a counterpart in monostatic radar. This report focuses on computer models of ideal systems and does not address the Tx–Rx synchronization problem. Separation of the signals propagating along the direct, specular, and scattered paths is another implementation issue that needs to be addressed in a bistatic system. Additionally, the resolution of bistatic radar systems degrades at large bistatic angles in all dimensions of the radar measurement: downrange, cross-range and Doppler.[4] The quantitative evaluation of the radar imaging system resolution, which forms the core of this investigation, is addressed in Sections 4 and 5.

To illustrate the problem of separating the three possible propagation paths between Tx and Rx, we show the range profile obtained for two bistatic geometries in Fig. 5. The simulations, performed by the AFDTD software (described in a later paragraph), assume that we transmit a short UWB impulse with 1.5-GHz bandwidth centered at 1.25 GHz. The target is an M15 landmine buried 2 cm under flat ground. The Tx and Rx are vertical dipoles placed 2 m above the ground and 5 m from the target horizontally. Note that when the bistatic angle is 45° (relatively close to monostatic geometry), there is very good separation between the returns corresponding to the three propagation mechanisms. However, for $\beta = 135°$, the separation is much smaller, although the large bandwidth still allows each peak to be distinguished in the range profile. It is apparent that for $\beta = 180°$ the specular and scattered paths would become identical and the target response could not be separated from the ground bounce.

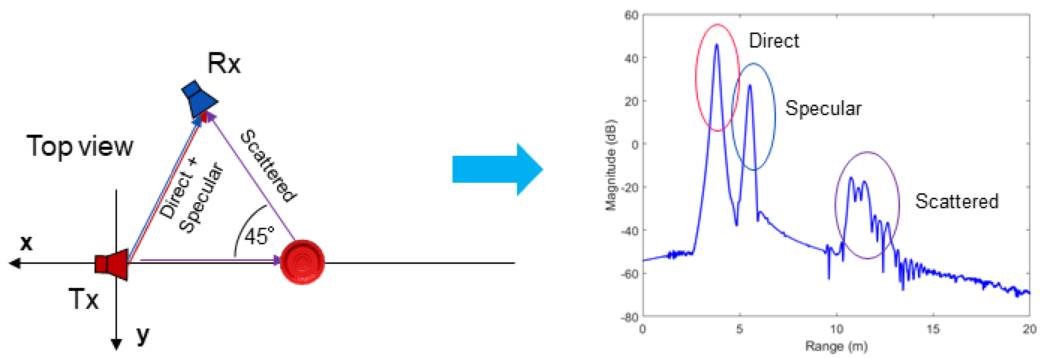

(a)

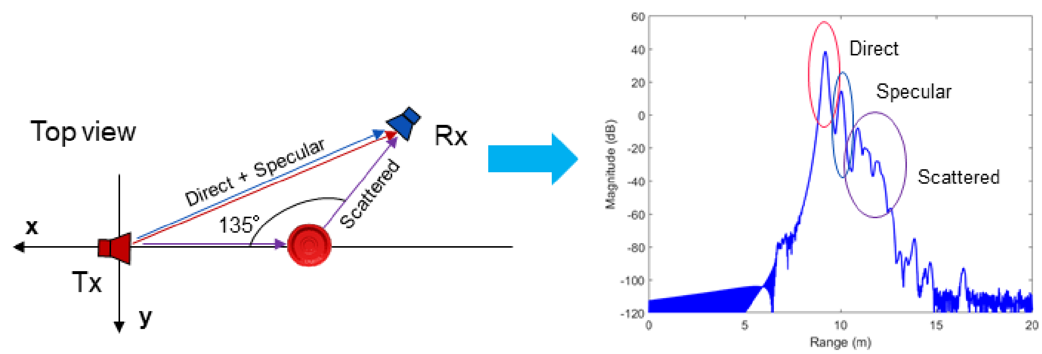

(b)

Fig. 5 Range profiles obtained in bistatic radar sensing of an M15 landmine, showing the three signal components, obtained for a bistatic angle of a) 45° and b) 135°

The imaging algorithm employed in this work is based on the matched filter method,[7] where the matched filter's transfer function is the conjugate phase of a point target response. Specifically, the complex intensity of an image pixel at position (x, y) in the ground plane is given by

$$I(x,y)=\frac{1}{NM}\sum_{n=1}^{N}\sum_{m=1}^{M}W(m,n)P(m,n)\exp\left(j\frac{2\pi f_m}{c}\left(R_{T,n}(x,y)+R_{R,n}(x,y)\right)\right), \quad (2)$$

where $P(m,n)$ is the radar signal obtained for the Tx–Rx pair index n at frequency index m, M stands for the number of frequencies, N stands for the number of Tx–Rx pairs taken into account in the image formation procedure, while $W(m,n)$

is a sidelobe-control window function depending on frequency and the Tx–Rx positions. The Tx- and Rx-pixel ranges are computed as

$$R_{T,n}(x,y)=\sqrt{\left(x-x_{T,n}\right)^2+\left(y-y_{T,n}\right)^2+z_{T,n}^2}\,, \tag{3a}$$

$$R_{R,n}(x,y)=\sqrt{\left(x-x_{R,n}\right)^2+\left(y-y_{R,n}\right)^2+z_{R,n}^2}\,, \tag{3b}$$

with the subscripts T and R denoting Tx and Rx, respectively (Fig. 6). Note that this imaging procedure is valid for any bistatic radar system with arbitrary aperture geometries and is equivalent to the backprojection algorithm, with the processing taking place in the frequency domain.

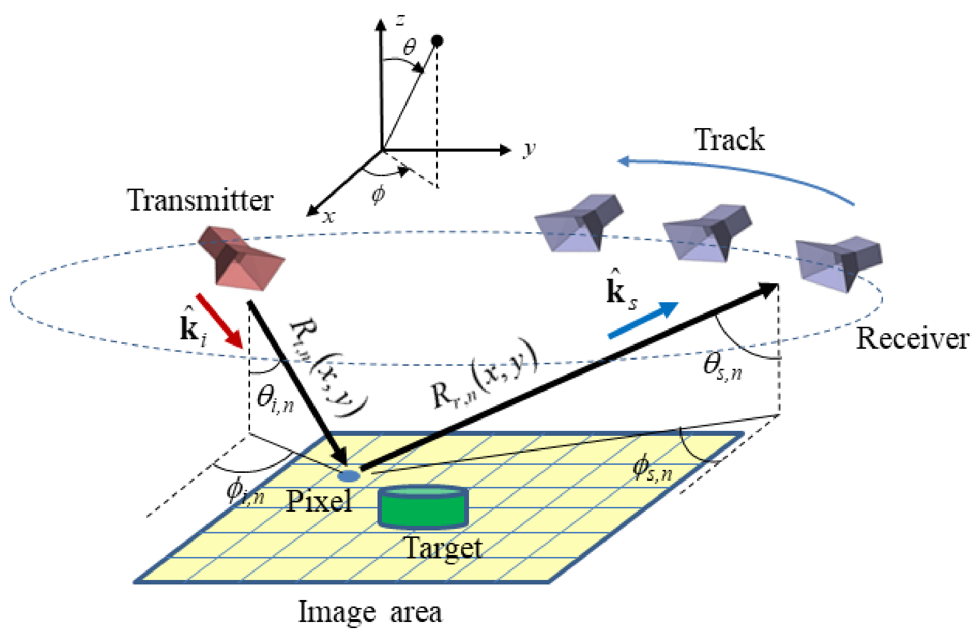

Fig. 6 Schematic representation of the bistatic radar imaging system for CEH applications, showing the relevant geometric elements

In Section 4 of this report, we investigate the PSF of the bistatic imaging system. For this purpose, the target is a point placed at (x_0, y_0) in the ground plane, and the radar received signal becomes

$$P(m,n)=\exp\left(-j\frac{2\pi f_m}{c}\left(R_{T,n}(x_0,y_0)+R_{R,n}(x_0,y_0)\right)\right). \tag{4}$$

Note that this procedure of PSF calculation ignores the amplitude variations of the point target response with the Tx and Rx positions.

The other images in Sections 4 and 5 are based on electromagnetic (EM) simulation data generated by the AFDTD software.[8] This software, developed entirely at ARL, relies on the finite-difference time-domain (FDTD) method, and was designed specifically to model radar configurations like those considered in this report. In Section 4 we use a near-field version of the code[9] where the Tx and Rx are embedded inside the computational domain. In Section 5 we use the far-field version of the same code, where the excitation is provided by a plane wave. The targets employed in these simulations are antitank landmines (further described in Section 3) buried in a lossy dielectric soil medium. Additionally, AFDTD allows the user to include ground surface clutter in modeling the radar scattering phenomena. We take advantage of this feature in Sections 3 and 5 of the report. To create the images described by Eq. 2, the AFDTD software provides the $P(m,n)$ complex signals over the entire range of frequencies and aperture positions.

3. Target and Clutter Signature in Bistatic Radar

3.1 Target RCS in Bistatic Radar

In this section, we discuss the numeric calculations of the bistatic RCS[10] of two targets representative for CEH applications: the M15 metallic antitank landmine and the TM62P2 plastic antitank landmine (Fig. 7). Both targets are shallow-buried (with the top surface at 2 cm below the air–ground interface) in wet soil, with complex dielectric constant $\varepsilon_r = 8 - j0.9$. The RCS values are computed as averages over frequencies extending from 0.5 to 3 GHz, which are typical for UWB radar systems employed in these applications. In terms of radar polarizations, we are interested in all possible combinations: vertical–vertical (V-V), horizontal–horizontal (H-H), vertical–horizontal (V-H), and horizontal–vertical (H-V). Note that, for bistatic radar, the V-H and H-V signatures are different (unlike the case of monostatic radar, where they are identical). Importantly, the target RCS in the specular scattering direction does not include the contribution of the ground bounce.

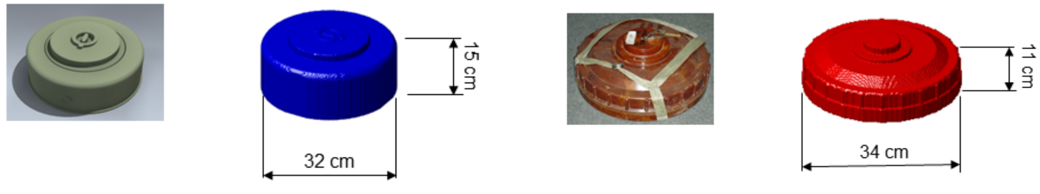

(a) (b)

Fig. 7 Photos and AFDTD computational meshes of the two targets modeled in this report: a) M15 metallic antitank landmine and b) TM62P2 plastic landmine

The fact that the targets are rotationally symmetric reduces the dimensions of the angular space over which the RCS needs to be evaluated. Thus, the Tx azimuth ϕ_i can be fixed to 0°, while the Rx azimuth ϕ_s is allowed to vary between 0° and 180°. However, the elevation angles of Tx and Rx need to vary independently. To keep the number of simulations below reasonable limits, we consider only four elevation angles for the Tx (75°, 65°, 55°, and 45°; note that 75° is closer to grazing than 45°), while the Rx elevation varies from 0° to 90°. The scattering angles (both ϕ_s and θ_s) vary in 5° increments.

Particular attention is given to the graphic representation of the bistatic RCS results over the angular space. Thus, each graph represents a 2-D surface (with the RCS in decibels-square-meter [dBsm]) where the Tx location is fixed and the two scattering angles are variable. A full 3-D representation of the RCS manifold should be painted on the surface of a sphere (more exactly, the surface of a quarter-sphere), as shown in Fig. 8a. However, since this 3-D representation cannot be properly laid out in the page and is difficult to interpret by the user, we chose to collapse it onto the horizontal (*x-y*) plane as shown in Fig. 8b. Note that in this polar-type plot the angular coordinate corresponds directly to ϕ_s, while the radial coordinate corresponds to $\sin\theta_s$ (so there is a nonlinear relationship between the radius and θ_s). The Tx angular coordinates are indicated in each plot by a black dot.

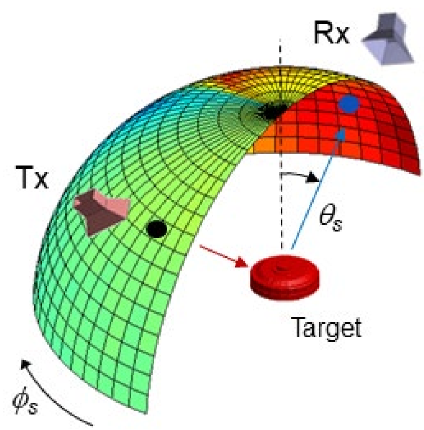

(a)

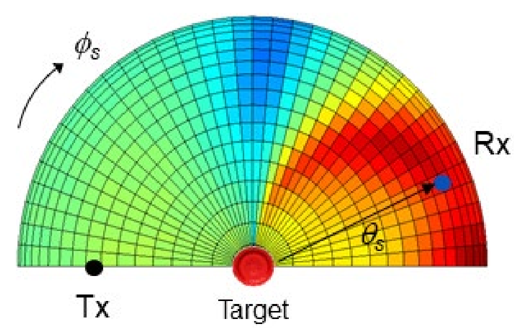

(b)

Fig. 8 Representation of the target's bistatic RCS as a function of the scattering azimuth and elevation angles: a) 3-D representation of the RCS surface and b) the RCS surface collapsed onto the horizontal plane

Figures 9–12 represent the RCS of the M15 metallic landmine for the four Tx elevations and the four polarization combinations. The same plots, this time for the TM62P2 plastic landmine, are shown in Figs. 13–16. One obvious feature in the co-polarization (V-V and H-H) graphs is that the largest RCS is obtained in the forward scattering direction (close to specular), with the effect being more pronounced for the M15 mine. In the same graphs, the smallest RCS is obtained when ϕ_s = 90°. While the V-V and H-H RCS plots display fairly similar patterns, the cross-polarization configurations (V-H and H-V) create patterns almost complementary to co-polarization: the RCS is maximum at ϕ_s = 90° and minimum in backscatter and specular direction.

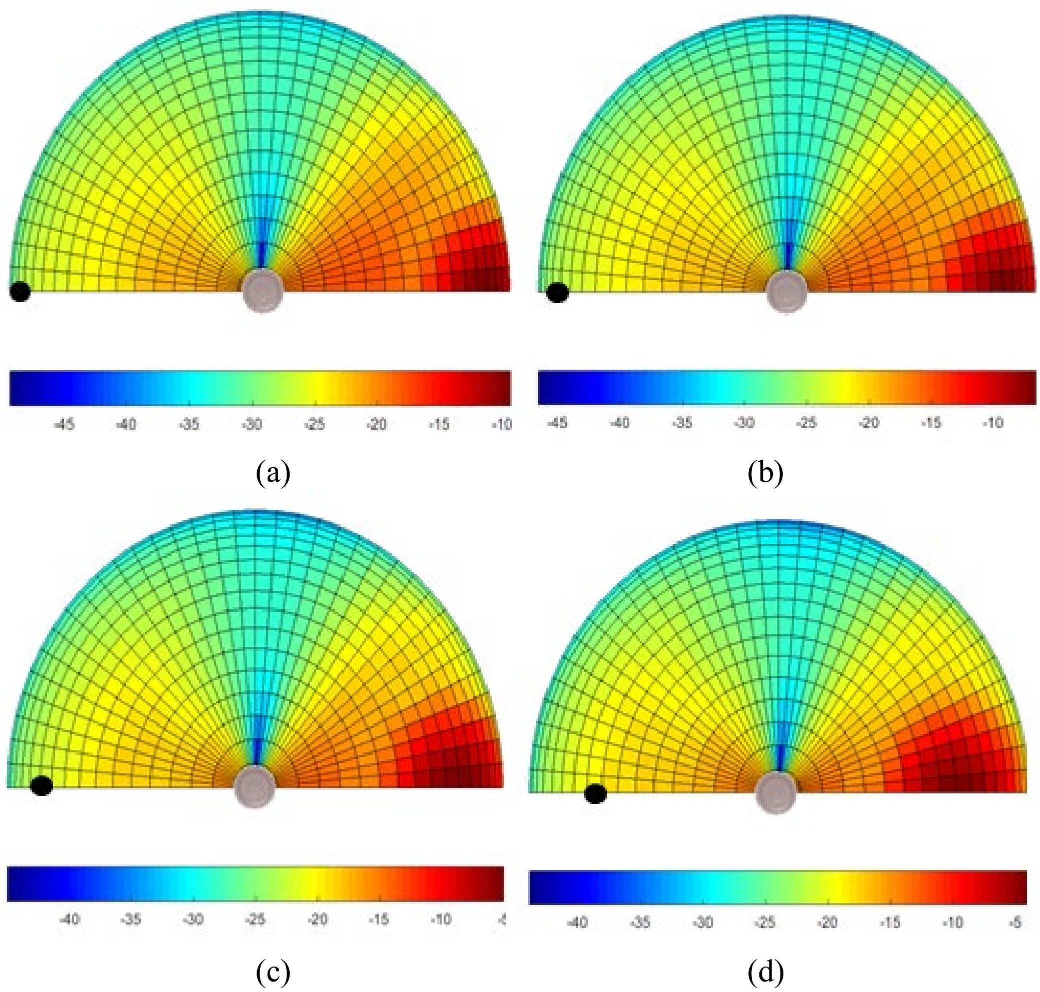

Fig. 9 Bistatic RCS of the M15 metallic landmine evaluated in dBsm, averaged between 0.5 and 3 GHz, for V-V polarization, ϕ_i = 0° and θ_i equal to a) 75°, b) 65°, c) 55°, and d) 45°

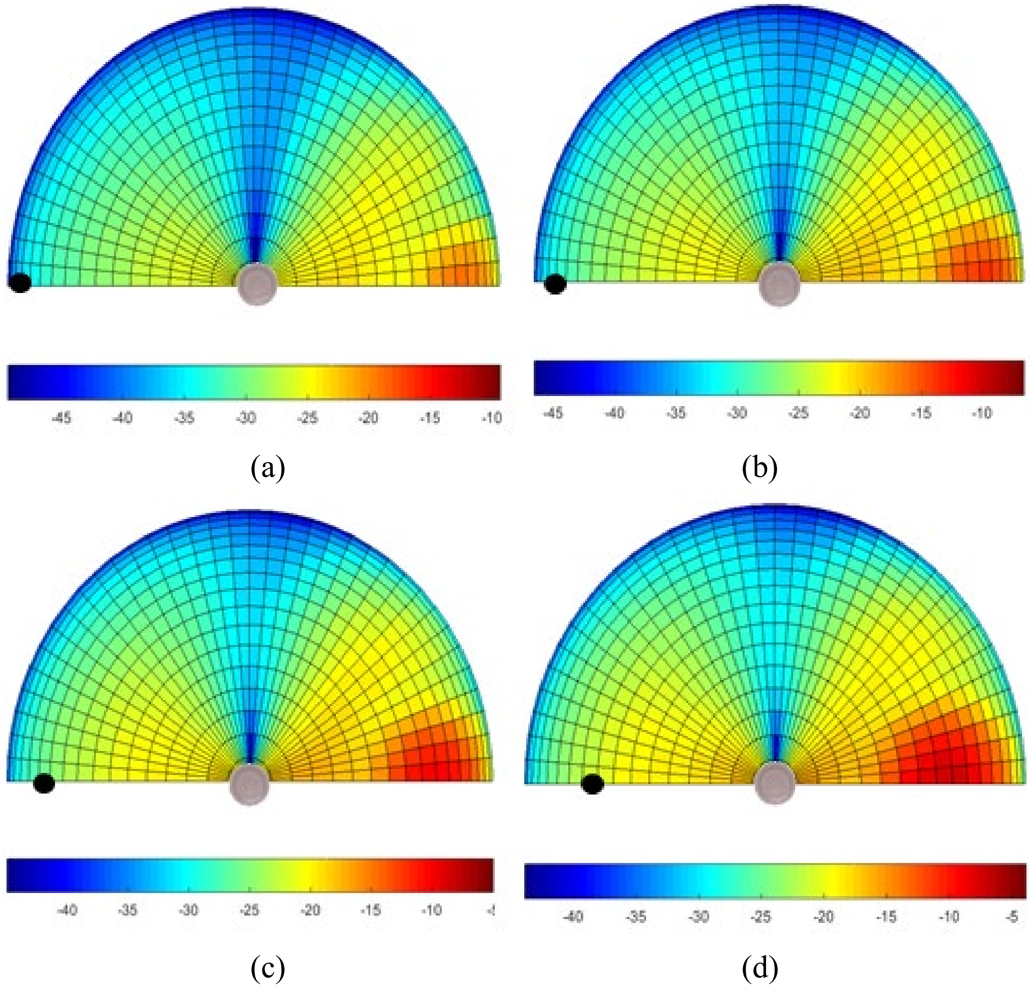

Fig. 10 Bistatic RCS of the M15 metallic landmine evaluated in dBsm, averaged between 0.5 and 3 GHz, for H-H polarization, $\phi_i = 0°$ and θ_i equal to a) 75°, b) 65°, c) 55°, and d) 45°

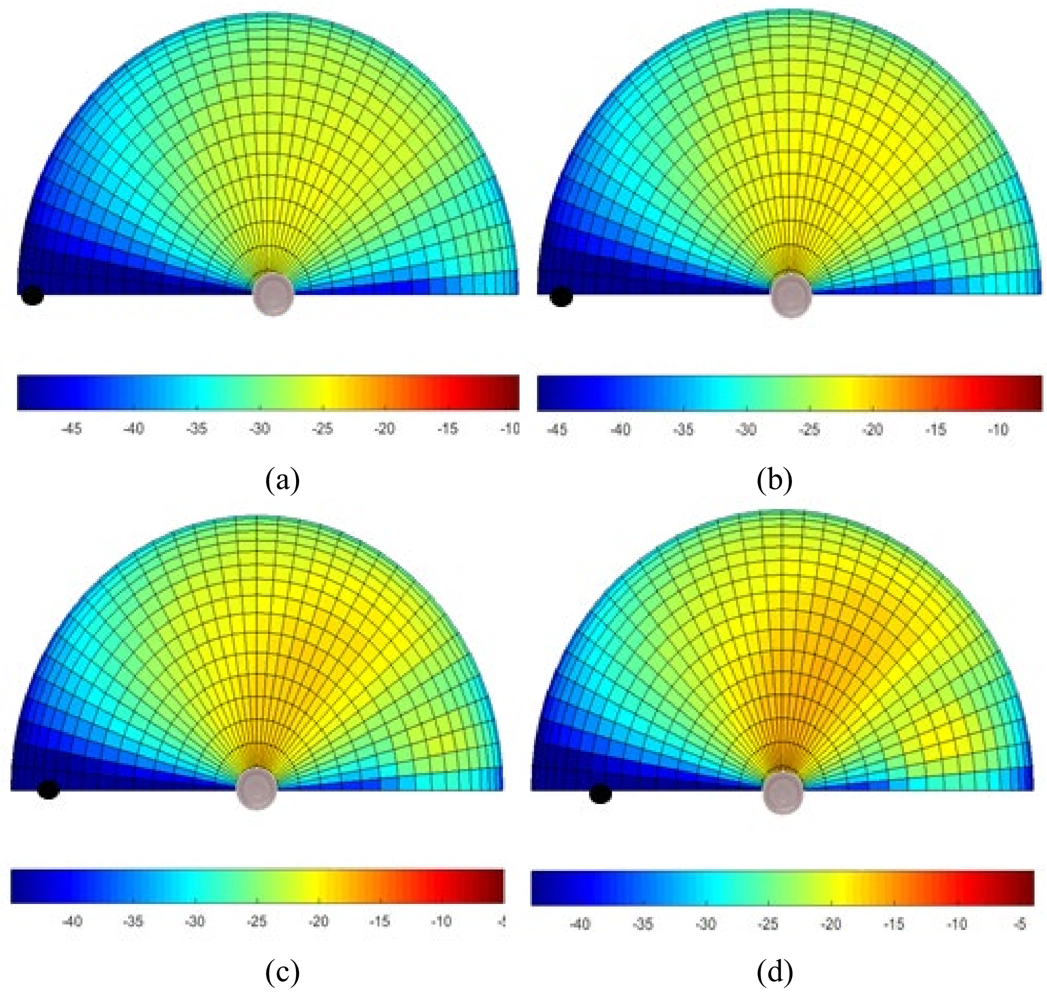

Fig. 11 Bistatic RCS of the M15 metallic landmine evaluated in dBsm, averaged between 0.5 and 3 GHz, for V-H polarization, $\phi_i = 0°$ and θ_i equal to a) 75°; b) 65°; c) 55°; d) 45°

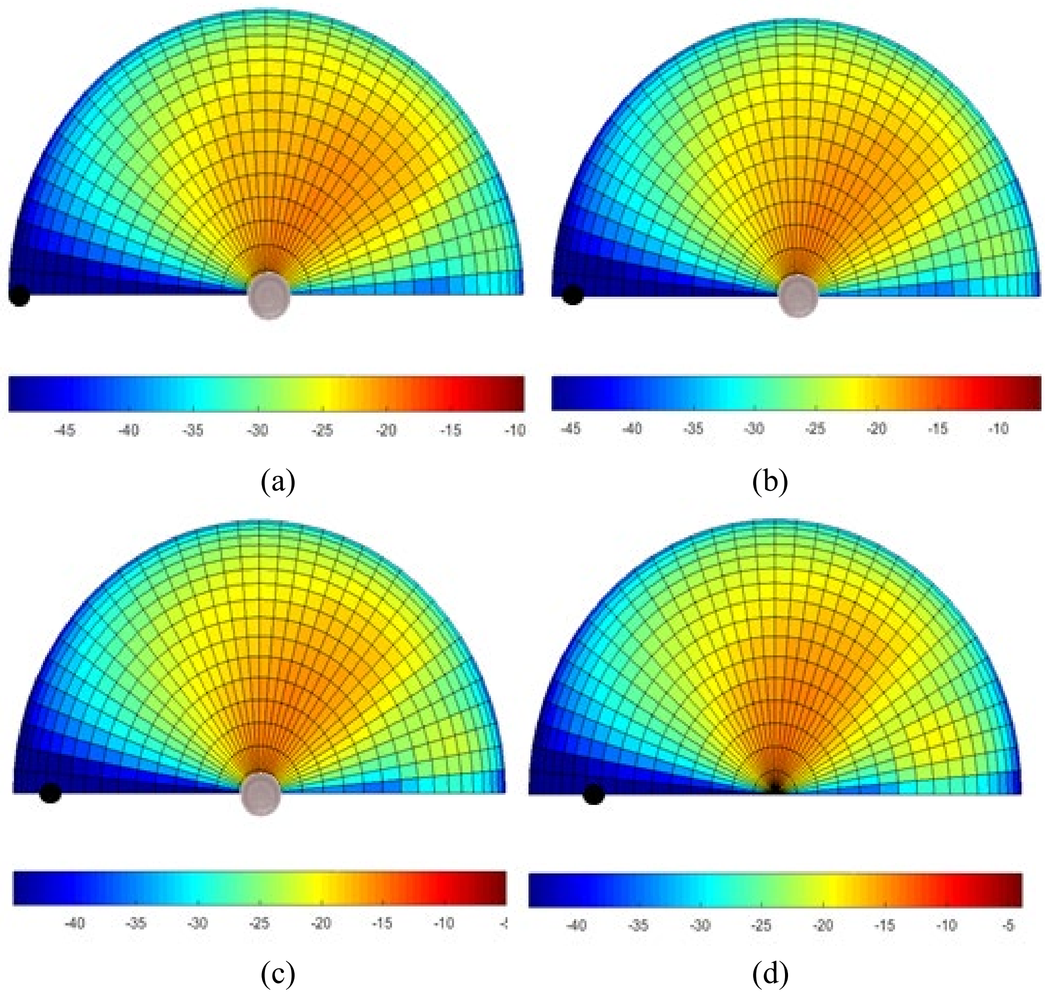

Fig. 12 Bistatic RCS of the M15 metallic landmine evaluated in dBsm, averaged between 0.5 and 3 GHz, for H-V polarization, $\phi_i = 0°$ and θ_i equal to a) 75°, b) 65°, c) 55°, and d) 45°

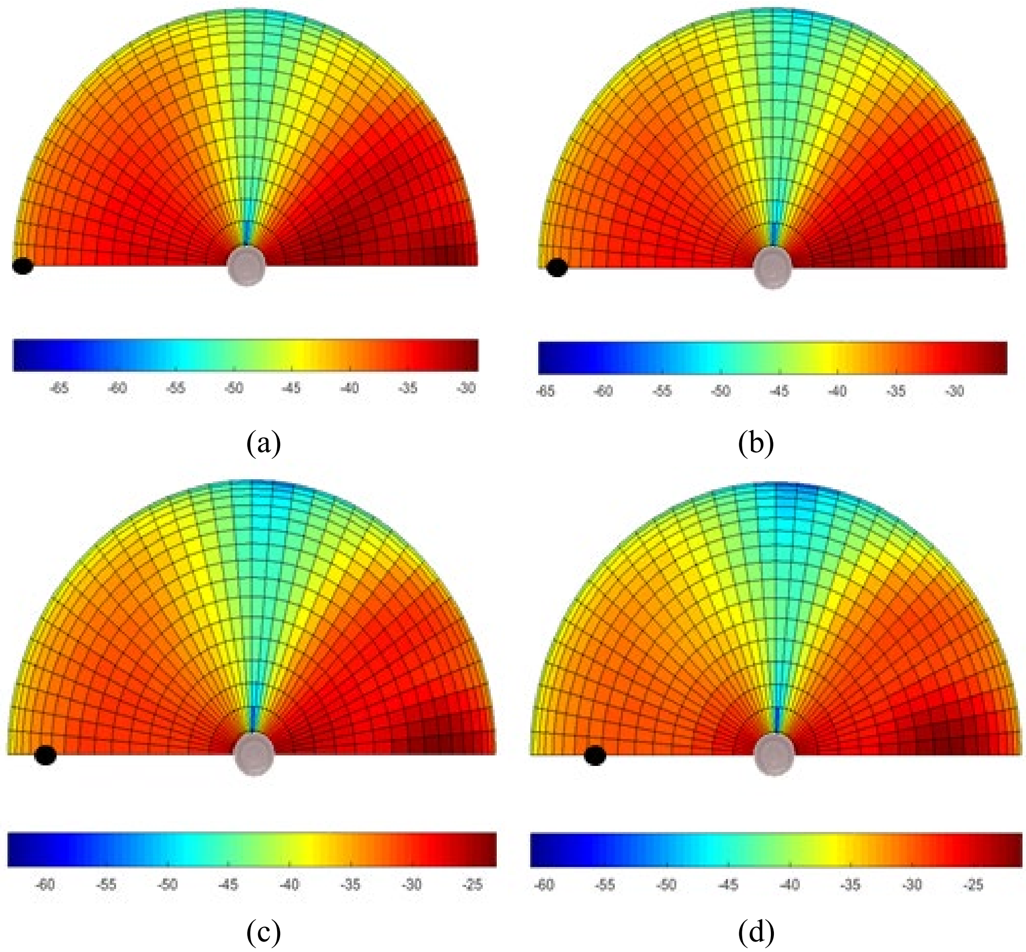

Fig. 13 Bistatic RCS of the TM62P2 plastic landmine evaluated in dBsm, averaged between 0.5 and 3 GHz, for V-V polarization, ϕ_i = 0° and θ_i equal to a) 75°, b) 65°, c) 55°, and d) 45°

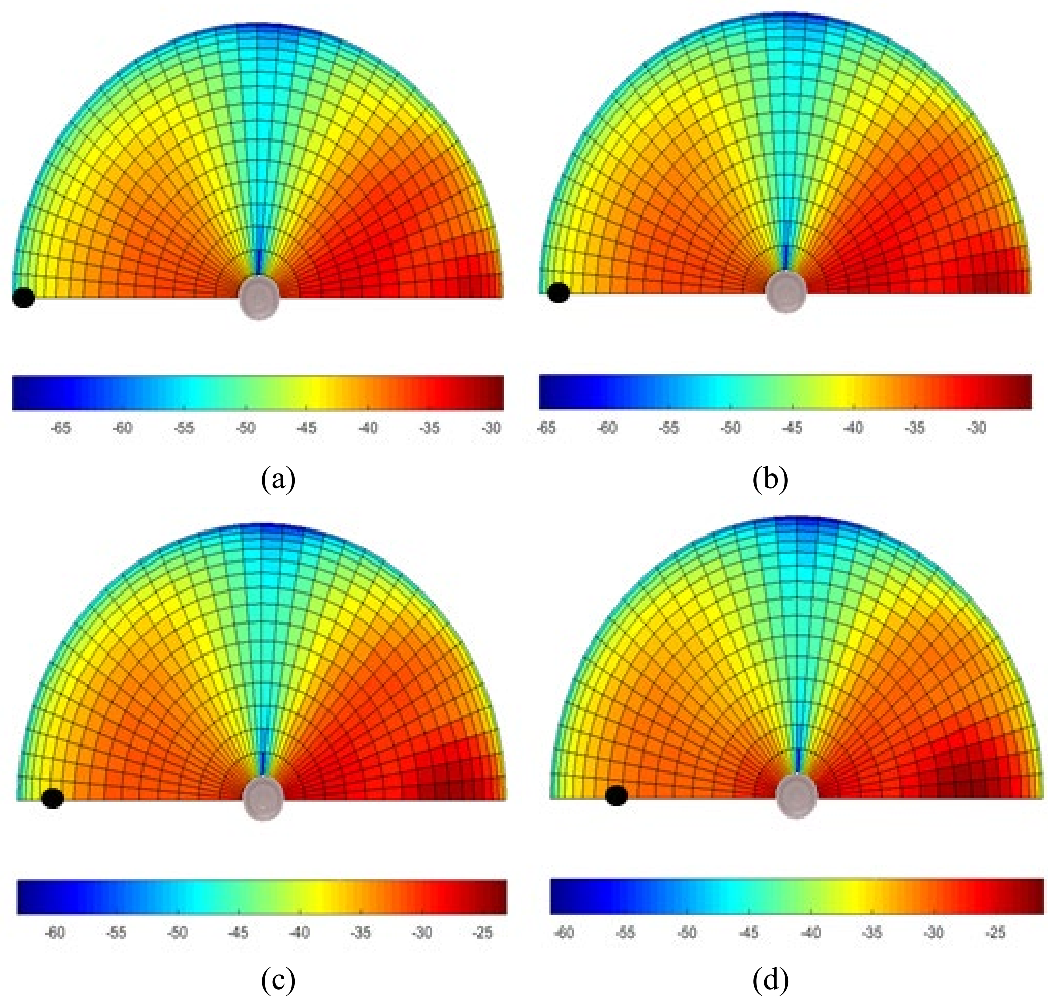

Fig. 14 Bistatic RCS of the TM62P2 plastic landmine evaluated in dBsm, averaged between 0.5 and 3 GHz, for H-H polarization, ϕ_i = 0° and θ_i equal to a) 75°, b) 65°, c) 55°, and d) 45°

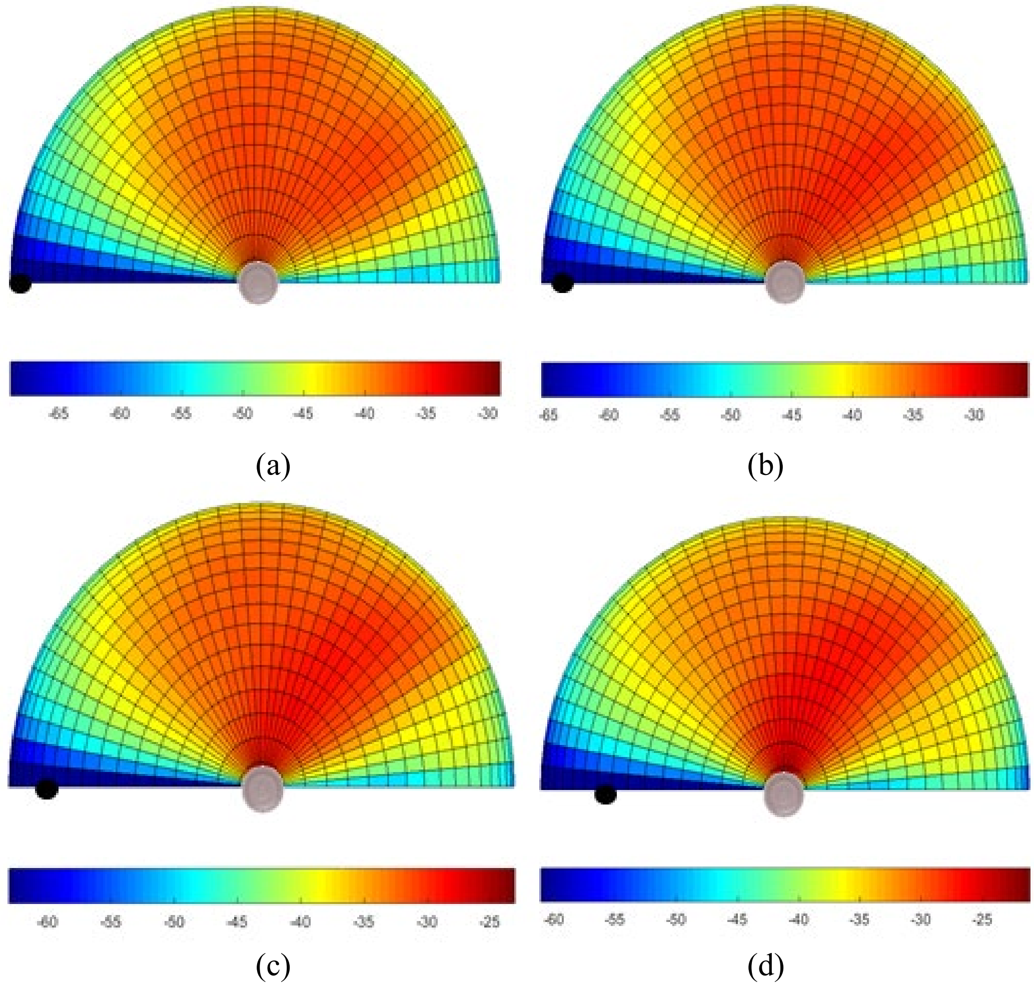

Fig. 15 Bistatic RCS of the TM62P2 plastic landmine evaluated in dBsm, averaged between 0.5 and 3 GHz, for V-H polarization, $\phi_i = 0°$ and θ_i equal to a) 75°, b) 65°, c) 55°, and d) 45°

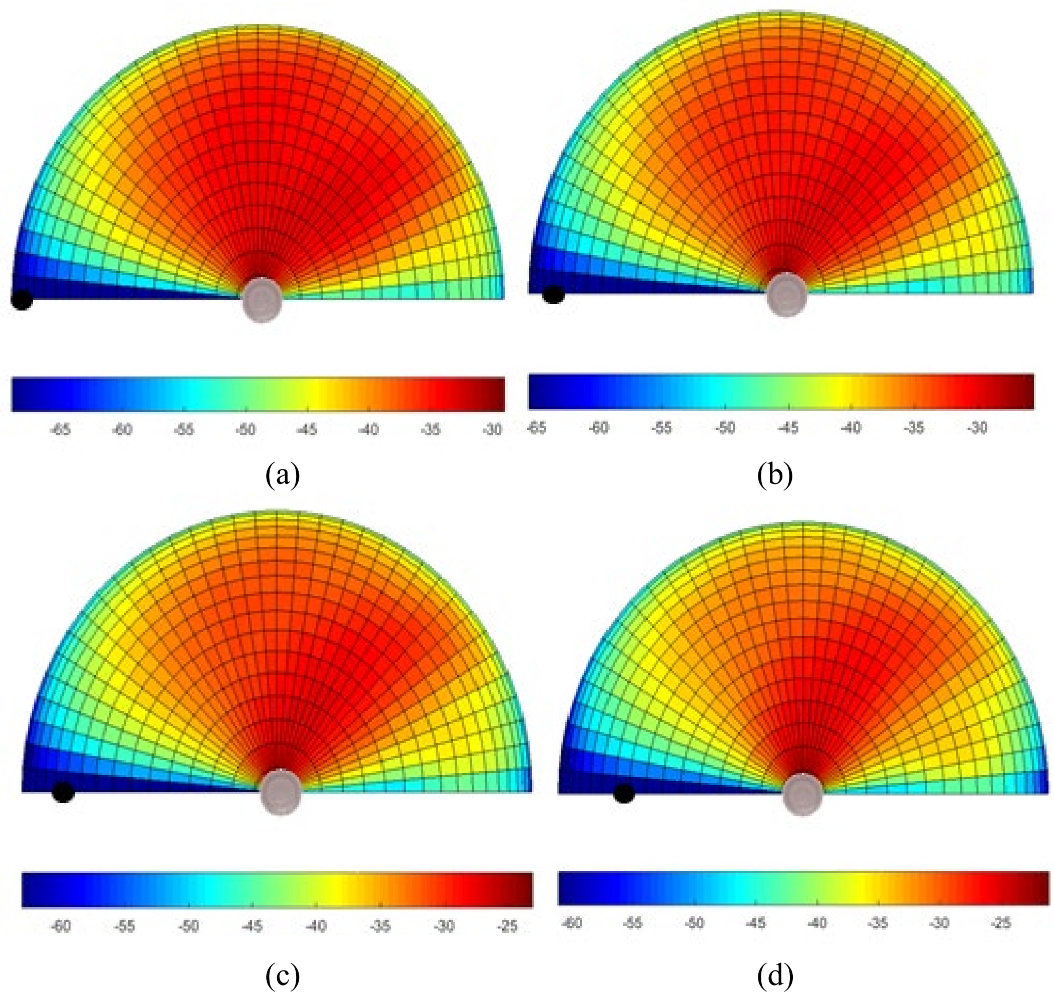

Fig. 16 Bistatic RCS of the TM62P2 plastic landmine evaluated in dBsm, averaged between 0.5 and 3 GHz, for H-V polarization, $\phi_i = 0°$ and θ_i equal to a) 75°, b) 65°, c) 55°, and d) 45°

It is of particular interest to find the angles $\left(\phi_s^{\max}, \theta_s^{\max}\right)$ where the maximum bistatic RCS occurs and to compare that value with the monostatic RCS obtained for the same Tx orientation. This is done in Table 1, where we list all these numbers for the two types of targets, V-V and H-H polarizations, and four different incidence angles. As expected, the maximum bistatic RCS is attained in the forward direction ($\phi_s^{\max} - \phi_i = 180°$); however, since we generally have $\theta_s^{\max} < \theta_i$, this direction differs slightly from specular. Note that the maximum bistatic RCS is always larger than the monostatic RCS, typically by 10 to 20 dB. Additionally, it is clear from these results that the plastic landmine generates a much weaker maximum return than the metallic one by at least 10 dB.

Table 1 Monostatic and maximum bistatic RCS of the M15 and TM62P2 landmines, averaged over frequencies between 0.5 and 3 GHz, for various polarizations and incidence angles. All RCS values are in dBsm.

θ_i	Pol	M15				TM62P2			
		RCS Mono-static	RCS Bistatic Max	ϕ_s Max	θ_s Max	RCS Mono-static	RCS Bistatic Max	ϕ_s Max	θ_s Max
75°	V-V	–29.3	–9.3	180°	60°	–41.1	–29.0	180°	55°
	H-H	–39.2	–18.6	180°	55°	–51.1	-32.1	180°	60°
65°	V-V	–25.0	–6.6	180°	60°	–36.0	–25.6	180°	55°
	H-H	–31.2	–13.5	180°	55°	–42.4	–27.3	180°	55°
55°	V-V	–22.1	–5.0	180°	50°	–32.7	–23.1	180°	50°
	H-H	–25.7	–9.8	180°	50°	–36.4	–24.0	180°	50°
45°	V-V	–19.0	–3.9	180°	45°	–29.9	–21.1	180°	40°
	H-H	–21.4	–6.9	180°	40°	–31.3	–21.7	180°	40°

3.2 Bistatic Clutter Return and Target-to-Clutter Ratio

Modeling the radar clutter return from rough terrain surfaces has been a long-time object of investigation for ARL researchers. The AFDTD software has been the main tool for these investigations. Extensive validation work[11,12] has been performed to confirm the accuracy of the AFDTD numerical results on general bistatic radar scattering from random rough dielectric surfaces. These results have been used in multiple radar performance studies seeking to predict the TCR of various radar systems.

To understand the impact of terrain clutter on the TCR for CEH applications of bistatic radar, we first investigate general characteristics of the bistatic scattering from random rough surfaces. As with the target models, all the simulations in this sections were performed with the AFDTD software. The simulation parameters (frequencies, bistatic angles, and soil dielectrics) are the same as in Section 3.1.

The terrain surfaces are modeled as 2-D random processes with Gaussian distribution. We consider processes with power-law spectrum (or exponential correlation function), independent of azimuth, which provide a good representation of natural terrain surfaces.[13] The equation describing this power spectral density is

$$W\left(k_\rho\right) = \pi\left(\frac{b}{2} - 1\right) h^2 L^2 \left(1 + \frac{k_\rho^2 L^2}{4}\right)^{-\frac{b}{2}}, \tag{5}$$

where k_ρ is the horizontal component of the wave vector $\mathbf{k}$, h is the root-mean square of the surface height, L is the surface correlation length and b is a power-law coefficient related to the fractal dimension of the surface (for an exponential correlation function we have $b = 3$). In our simulations we take $h = 3$ mm and $L = 5$ cm, as these are numbers typical for the surface of a dirt road. The bistatic radar scattering return from a rough surface is characterized by the scattering coefficient σ^0, which represents average RCS per unit area.[13] This quantity is formally defined by the following:

$$\sigma^0 = \frac{4\pi r^2}{A}\left\langle\left|\frac{E^s(\mathbf{r}) - \langle E^s(\mathbf{r})\rangle}{E^i}\right|^2\right\rangle, \tag{6}$$

where $\mathbf{r}$ is the range from the illuminated surface patch to the radar receiver (assumed in the far field), A is the surface patch area, E^i and E^s are the complex incident and scattered fields measured on the surface and at the radar receiver, respectively, and the symbol $\langle\ \rangle$ represents the ensemble averaging operator.

To obtain the averages, 50 Monte Carlo realizations of the random process were run for each set of radar parameters. Importantly, σ^0 describes the incoherent scattering from the surface; that is, the specular reflection from the surface is not included in the results. As in the case of target RCS, we compute average values of σ^0 over the entire frequency band. Note that the same symmetry rules with respect to the incidence and scattering angles apply to both sets of radar signature metrics (target RCS and clutter σ^0).

The results of rough surface scattering bistatic returns are shown in Figs. 17–20, for the four polarization combinations and four incidence angles mentioned in Section 3.1, in the same graphic format as the target RCS (the units in the color bar are in decibels [dB]). Note that for H-H, H-V, and V-H polarization, the angular variation of σ^0 displays a very similar pattern with the target RCS. Thus, the $\phi_s = 90°$ direction corresponds to the minimum return in H-H polarization and maximum return in cross-polarization, while the opposite is true for the backscatter and specular directions. However, the clutter return map in V-V polarization presents a very peculiar bistatic pattern, characterized by a low-magnitude "valley" corresponding roughly to scattering angles satisfying the relation $\phi_s - \phi_i = 90^\circ + \theta_s \sin\theta_i$. Although no easy intuitive explanation exists for this phenomenon, the effect is consistent with the formulas describing the first-order small perturbation method (SPM) for rough surface scattering of EM waves.[14] In fact, the results in Figs. 17–20 are very similar to those reported by Johnson and Ouellette,[15] based on first-order SPM.

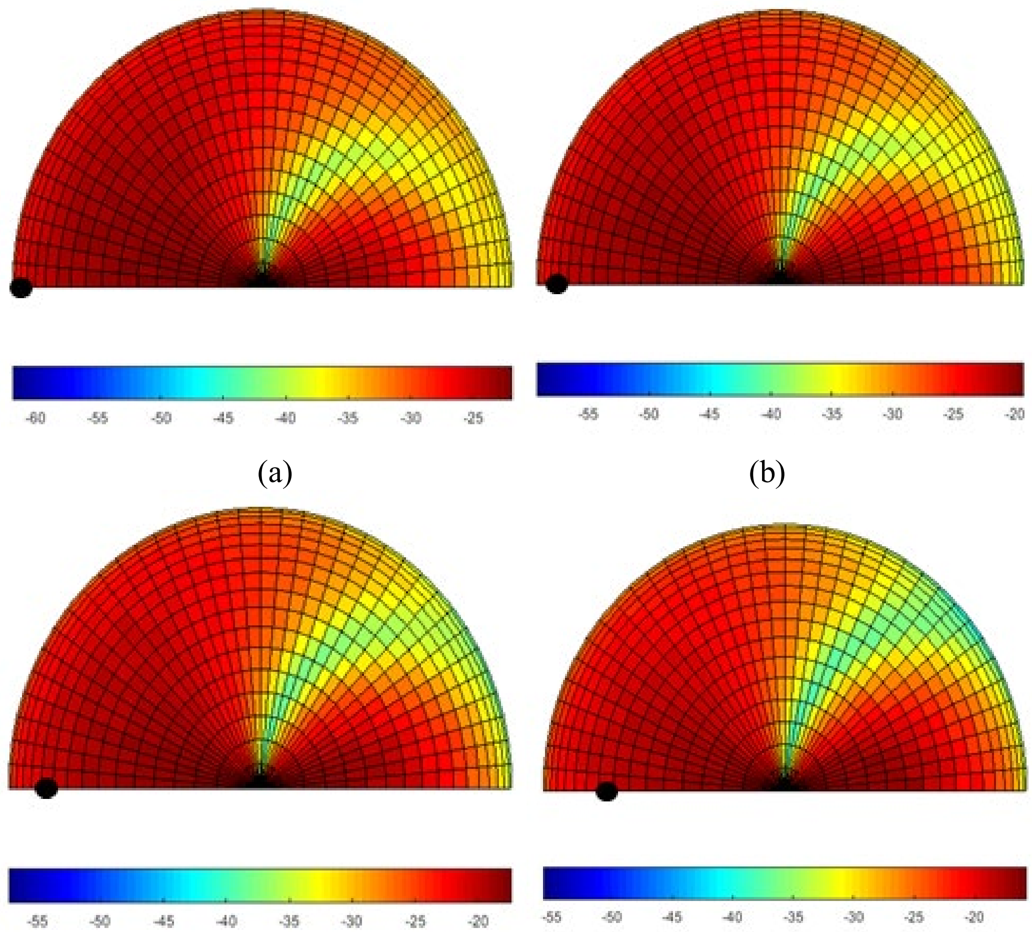

(a) (b)

(c) (d)

Fig. 17 Bistatic scattering coefficient σ^0 of an exponentially correlated rough surface with h = 3 mm and L = 5 cm, evaluated in dB, averaged between 0.5 and 3 GHz, for V-V polarization, and θ_i equal to a) 75°, b) 65°, c) 55°, and d) 45°

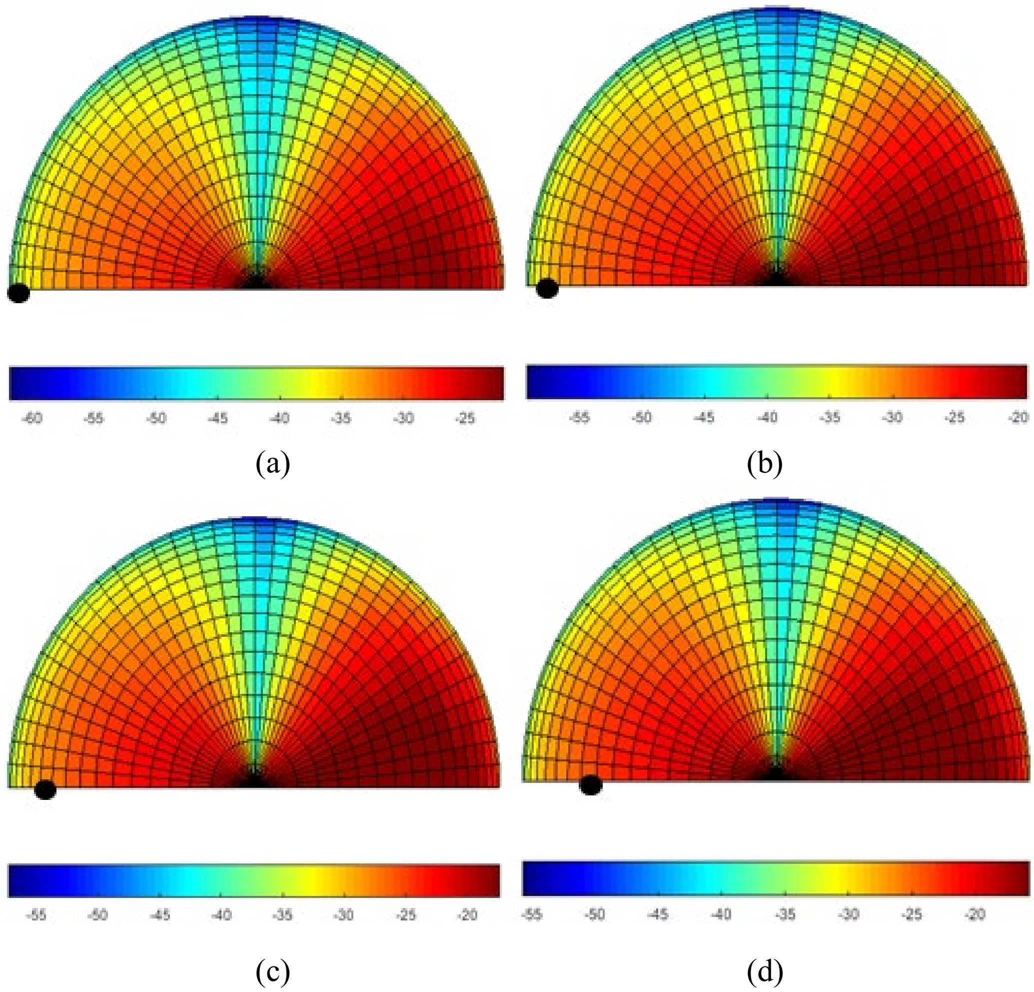

Fig. 18 Bistatic scattering coefficient σ^0 of an exponentially correlated rough surface with h = 3 mm and L = 5 cm, evaluated in dB, averaged between 0.5 and 3 GHz, for H-H polarization, and θ_i equal to a) 75°, b) 65°, c) 55°, and d) 45°

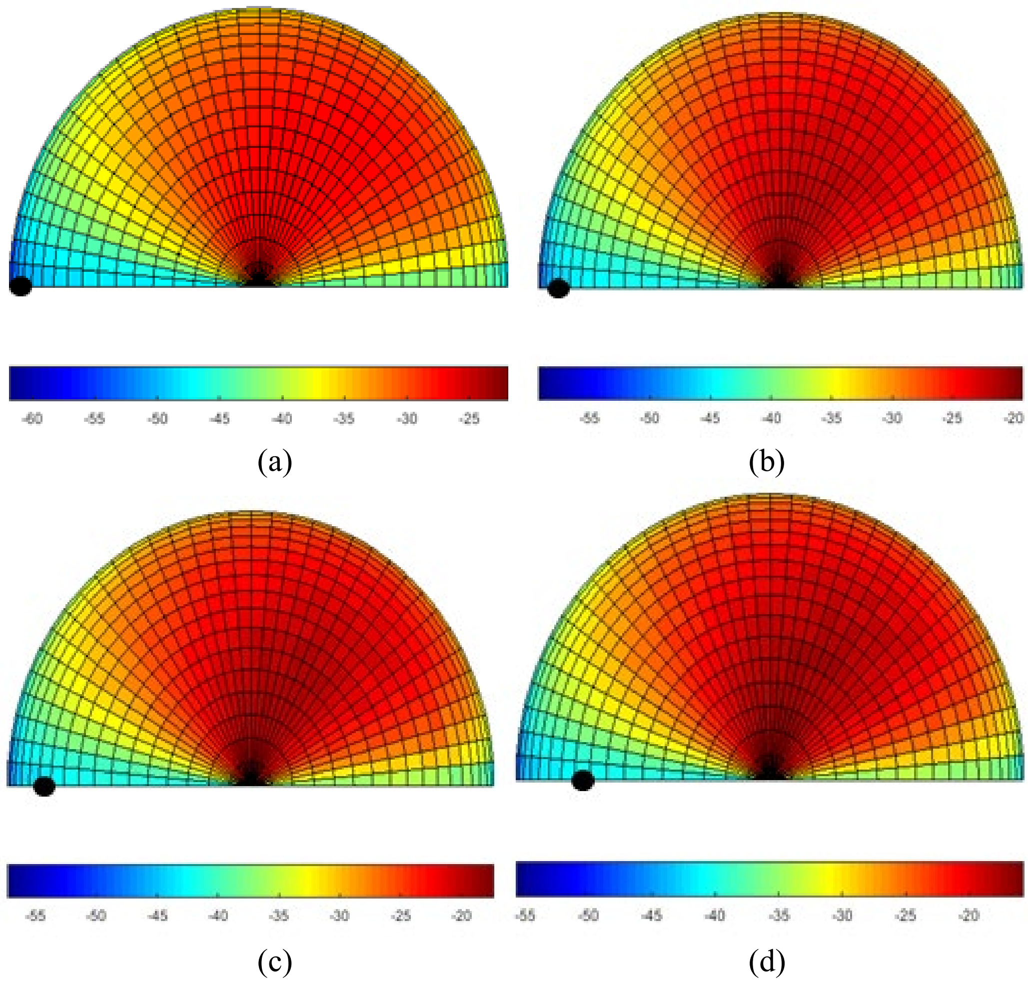

Fig. 19 Bistatic scattering coefficient σ^0 of an exponentially correlated rough surface with h = 3 mm and L = 5 cm, evaluated in dB, averaged between 0.5 and 3 GHz, for V-H polarization, and θ_i equal to a) 75°, b) 65°, c) 55°, and d) 45°

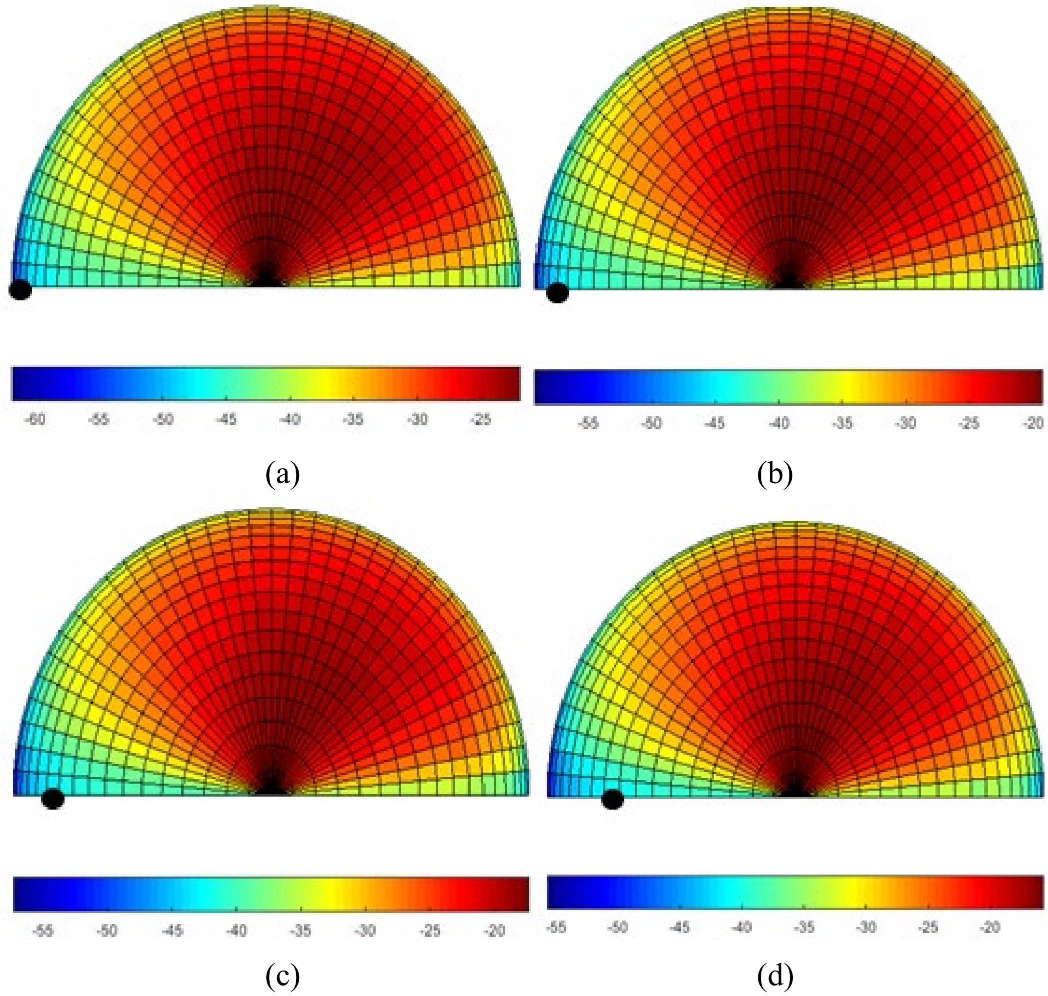

Fig. 20 Bistatic scattering coefficient σ^0 of an exponentially correlated rough surface with h = 3 mm and L = 5 cm, evaluated in dB, averaged between 0.5 and 3 GHz, for H-V polarization, and θ_i equal to a) 75°, b) 65°, c) 55°, and d) 45°

The evaluation of the target RCS (denoted by σ_{target}) and the surface clutter scattering coefficient (denoted by $\sigma^0_{clutter}$) allows us to predict the TCR as one of the key performance parameters for a given CEH radar sensing scenario. In a radar image, where the detection process is performed pixel by pixel, we are interested in the average TCR for the image resolution cell. This is computed by the following formula:

$$\mathrm{TCR} = \frac{\sigma_{target}}{\sigma^0_{clutter} A_{RC}}, \tag{7}$$

where A_{RC} is the area of the image resolution cell. The major complication arising in the case of bistatic radar systems is that the resolution cell size changes with the set of aspect angles according to the equation[4]

$$A_{RC} = \frac{c\lambda R_R}{2BD_R \cos\delta \cos^2\frac{\beta}{2}}, \tag{8}$$

where c is the speed of light, λ is the wavelength at the center frequency, R_R is the range from pixel to radar receiver, B is the signal bandwidth, and D_R is the receiver aperture length. This formula assumes that the bistatic radar system involves only one Tx, and the Rx aperture (physical or synthetic) is oriented perpendicular to the Rx line of sight (LOS). The angles β and δ were defined in Fig. 2c and can be calculated as a function of $(\phi_i, \theta_i, \phi_s, \theta_s)$ using the following formulas:

$$\cos^2\frac{\beta}{2} = \frac{1}{2}\left(1 + \cos\theta_i \cos\theta_s + \sin\theta_i \sin\theta_s \cos(\phi_i - \phi_s)\right), \tag{9a}$$

$$\cos\delta = \sqrt{1 - \frac{(\cos\theta_i + \cos\theta_s)^2}{4\cos^2\frac{\beta}{2}}}. \tag{9b}$$

Since δ is smaller than 90°, we always keep the positive solution of the square root in Eq. 9b. As an example, we represented the values of A_{RC} as a function of the angles (ϕ_s, θ_s), when ϕ_i = 0° and θ_i = 65°, in Fig. 21. In this figure, the units in the color bar are in dBsm. Other radar system parameters are: B = 2.5 GHz, λ = 0.17 m, R_R = 20 m, and D_R = 2 m. This plot clearly indicates that the best resolution (smallest A_{RC}) is obtained in the backscatter direction, while the worst resolution (largest A_{RC}) corresponds to the specular direction, with a dynamic range of 20 dB between the two.

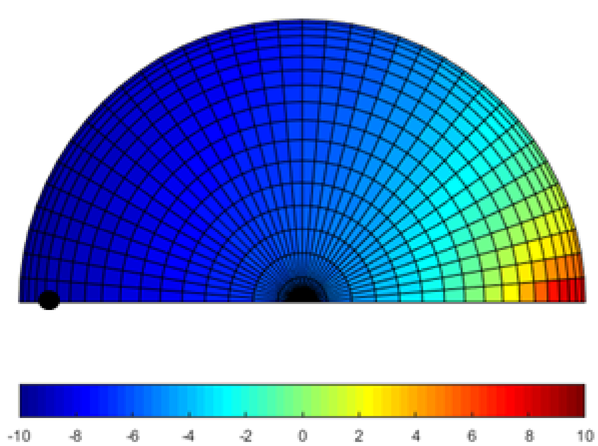

Fig. 21 Resolution cell area for a bistatic radar imaging system with ϕ_i = 0° and θ_i = 65°, as function of the scattering angles ϕ_s and θ_s

An interesting interpretation of the resolution variation with the aspect angles in bistatic radar can be made by drawing an analogy with monostatic SAR systems operating at a slant and a squint angle.[16] Thus, the bisector of the bistatic angle corresponds directly to the LOS in monostatic SAR. Furthermore, the bistatic angle $\frac{\beta}{2}$ is the analog (in a loose sense) of the squint angle in monostatic SAR, whereas the angle δ corresponds to the slant angle. As is well known in the theory of traditional SAR, imaging in a slanted and squinted geometry increases the resolution cell size by a factor inversely proportional to the cosines of those two angles.[16] A further analysis of the bistatic imaging radar system resolution is presented in Section 5.

The variations of the three parameters (σ_{target}, $\sigma^0_{clutter}$, and A_{RC}) are combined in Eq. 7 to obtain the TCR maps. These are displayed in Figs. 22 and 23 for the M15 metallic landmine and in Figs. 24 and 25 for the TM62P2 plastic landmine. Note that these plots characterize only the co-polarization combinations. For the cross-polarization channels, we limit our graphics to the $\theta_i = 65°$ case only, as shown in Figs. 26 (for M15) and 27 (for TM62P2). Table 2 contains the angles $\left(\phi_s^{\max}, \theta_s^{\max}\right)$ where the maximum bistatic TCR occurs, the numeric value of this maximum TCR, as well the monostatic TCR obtained for the same Tx orientations.

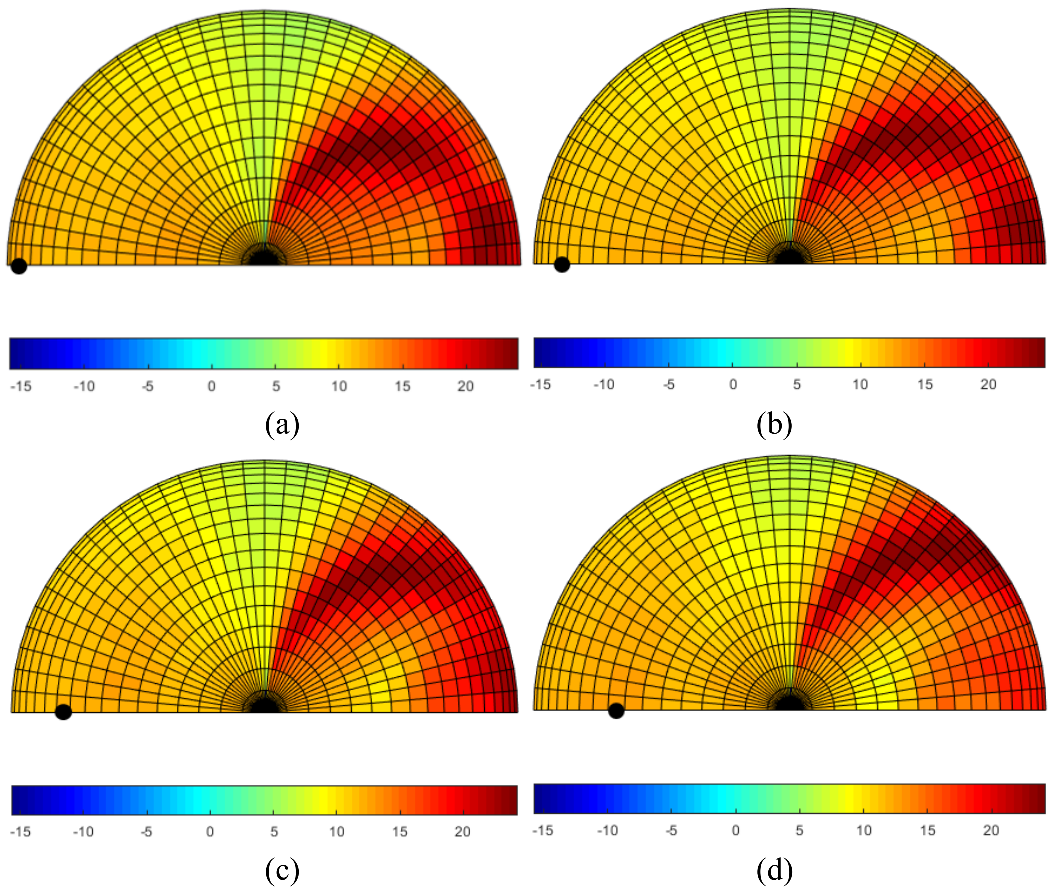

Fig. 22 Bistatic TCR of the M15 metallic landmine in the presence of rough surface clutter, evaluated in dB, averaged between 0.5 and 3 GHz, for V-V polarization, ϕ_i = 0° and θ_i equal to a) 75°, b) 65°, c) 55°, and d) 45°

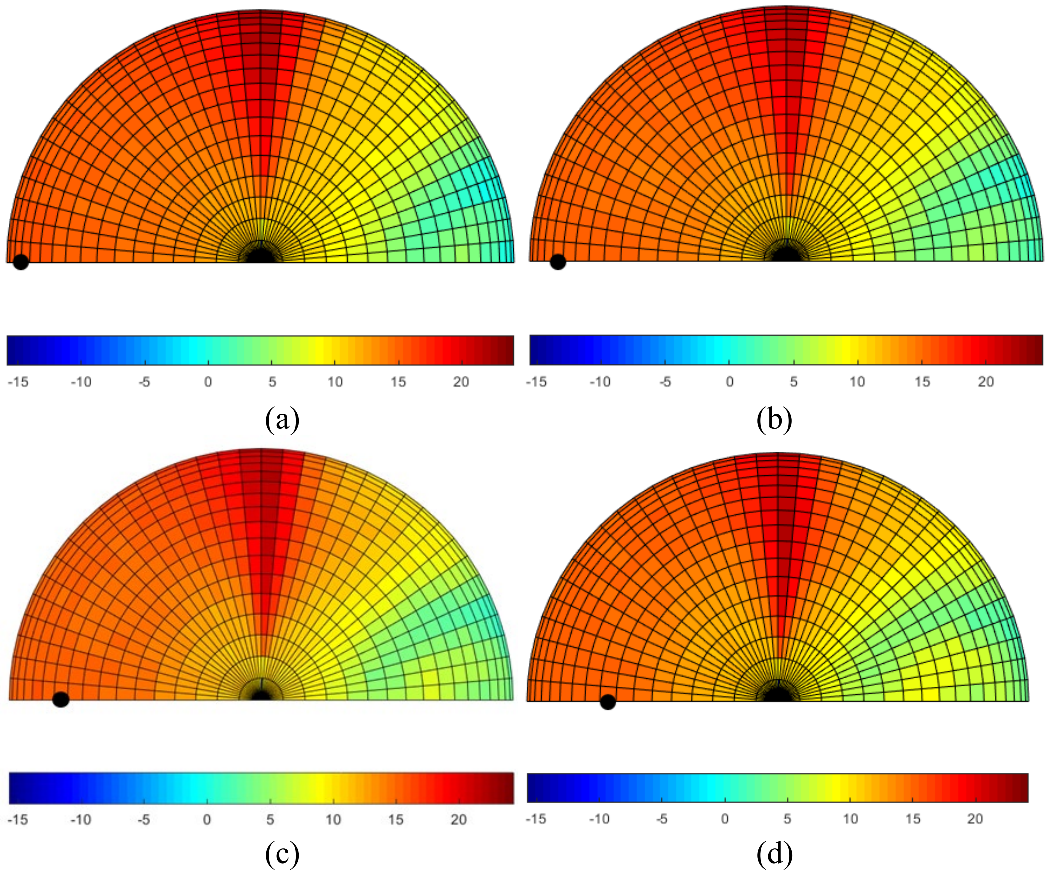

Fig. 23 Bistatic TCR of the M15 metallic landmine in the presence of rough surface clutter, evaluated in dB, averaged between 0.5 and 3 GHz, for H-H polarization, ϕ_i = 0° and θ_i equal to a) 75°, b) 65°, c) 55°, and d) 45°

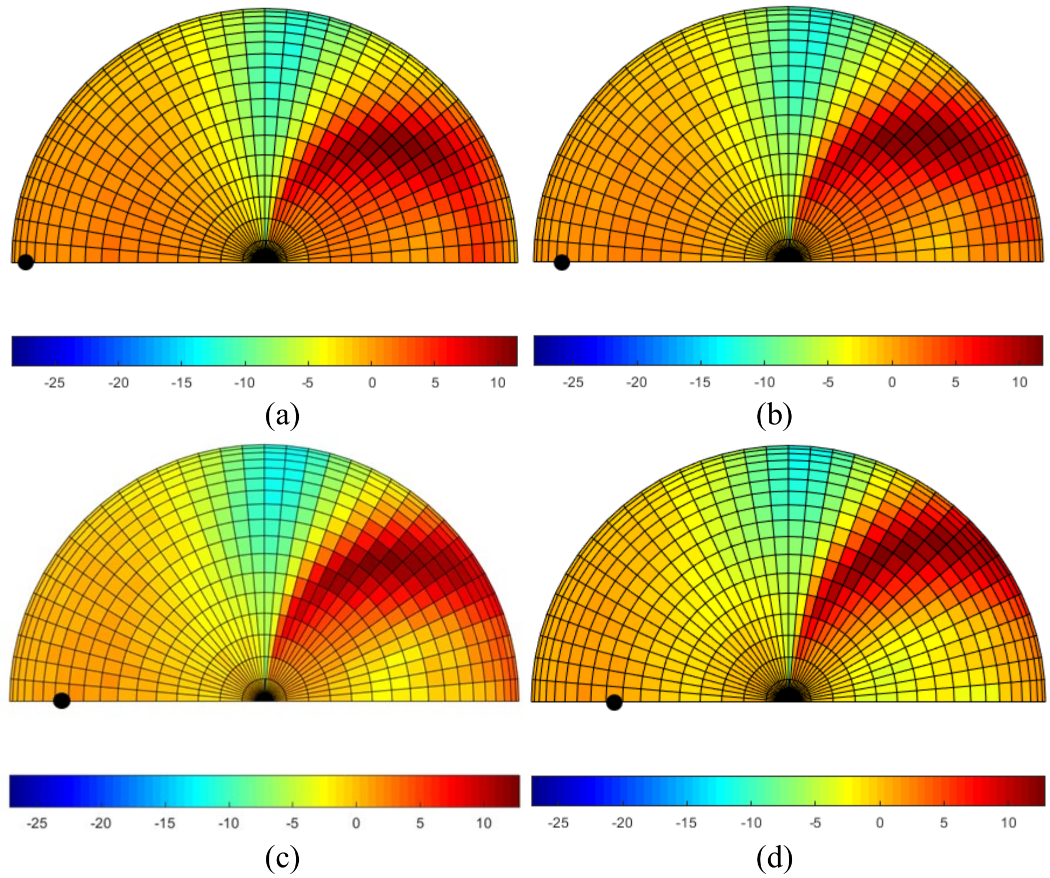

Fig. 24 Bistatic TCR of the TM62P2 plastic landmine in the presence of rough surface clutter, evaluated in dB, averaged between 0.5 and 3 GHz, for V-V polarization, $\phi_i = 0°$ and θ_i equal to a) 75°, b) 65°, c) 55°, and d) 45°

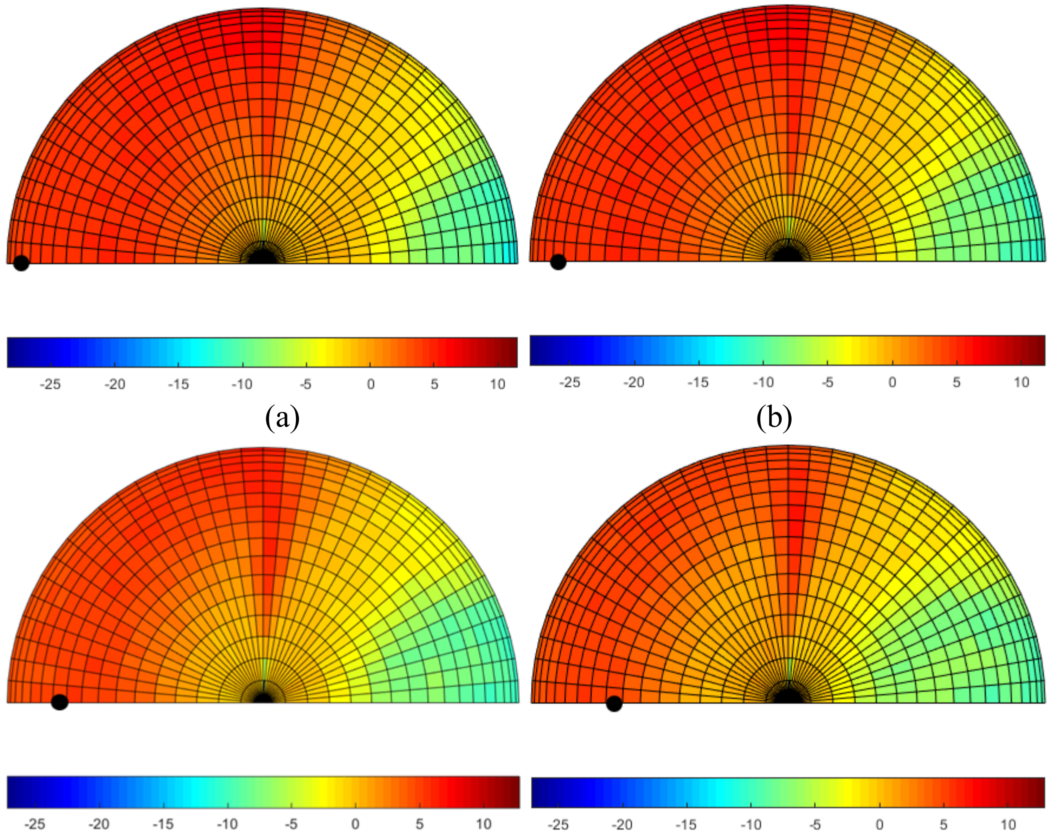

(a) (b)

(c) (d)

Fig. 25 Bistatic TCR of the TM62P2 plastic landmine in the presence of rough surface clutter, evaluated in dB, averaged between 0.5 and 3 GHz, for V-V polarization, ϕ_i = 0° and θ_i equal to a) 75°, b) 65°, c) 55°, and d) 45°

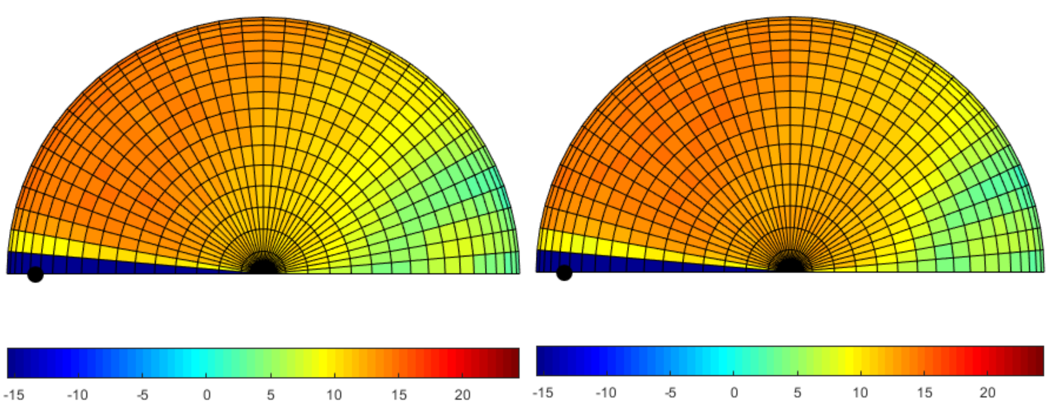

(a) (b)

Fig. 26 Bistatic TCR of the M15 metallic landmine in the presence of rough surface clutter, evaluated in dB, averaged between 0.5 and 3 GHz, for ϕ_i = 0°, θ_i = 65°: a) V-H polarization and b) H-V polarization

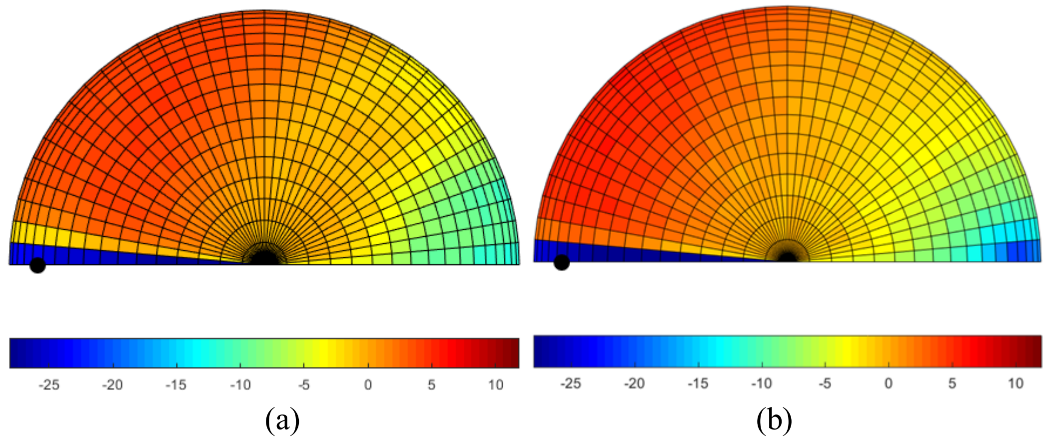

Fig. 27 Bistatic TCR of the TM62P2 landmine in the presence of rough surface clutter, evaluated in dB, averaged between 0.5 and 3 GHz, for ϕ_i = 0°, θ_i = 65°: a) V-H polarization and b) H-V polarization

Table 2 Monostatic and maximum bistatic TCR of the M15 and TM62P2 landmines in the presence of terrain clutter, averaged over frequencies between 0.5 and 3 GHz, for various polarizations and incidence angles. All TCR values are in dB.

θ_i	Pol	M15				TM62P2			
		TCR Mono-static	TCR Bistatic Max	ϕ_s Max	θ_s Max	TCR Mono-static	TCR Bistatic Max	ϕ_s Max	θ_s Max
75°	V-V	12.0	24.1	135°	40°	0.3	11.6	135°	40°
	H-H	15.5	22.6	90°	85°	3.6	7.0	85°	60°
65°	V-V	11.8	24.4	125°	35°	0.8	11.9	135°	45°
	H-H	15.6	22.5	90°	80°	4.4	7.1	85°	70°
55°	V-V	11.7	24.3	125°	40°	1.1	12.8	130°	45°
	H-H	15.5	21.9	90°	60°	4.9	6.6	85°	80°
45°	V-V	12.5	24.2	120°	40°	1.5	12.9	120°	40°
	H-H	15.3	22.1	90°	45°	5.3	7.1	90°	45°

A cursory look at the results in Table 2 indicates that the high TCR orientations generally correspond to the low $\sigma^0_{clutter}$ regions. Thus, for H-H polarization, we obtain maximum TCR around ϕ_s = 90°, while for V-V polarization, we obtain maximum TCR in the low-clutter "valley" described by $\phi_s - \phi_i = 90^\circ + \theta_s \sin\theta_i$. On the other hand, the specular direction (where the target RCS is maximum) exhibits poor TCR, because of the loss of image resolution at those bistatic scattering angles.

In absolute terms, the maximum TCR values are higher in V-V than H-H for the plastic mine and about the same for the metallic mine. With respect to the incidence elevation angle θ_i, the TCR generally increases as we approach grazing (larger θ_i), although this trend is fairly weak. Note that a similar trend is obtained in the monostatic configuration. For the cross-polarization cases, the largest TCR is achieved close to the backscatter direction (although not exactly in backscatter), where the clutter is weak. However, that region corresponds to very weak target signature as well; consequently, operating the radar system in such a configuration may become thermal-noise-limited rather than clutter-limited. As a reminder, the classic radar detection theory for nonfluctuating targets predicts a 95% probability of detection and a 10^{-6} probability of false alarm when the signal-to-interference ratio (in our case, the TCR) is 13 dB.[7]

The partial conclusion we draw so far from the TCR performance analysis of the bistatic imaging radar system is that certain bistatic sensing geometries can offer significant improvements in this metric compared with monostatic radar. The difference between the two depends on the target type and polarization and less on the incidence elevation angle. The results in Table 2 show a marked TCR increase (of at least 10 dB) for V-V polarization, while the H-H polarization improvement is more muted. Another important finding is that the maximum TCR for V-V polarization is achieved around $\phi_s - \phi_i$ = 135°, while for H-H this happens around $\phi_s - \phi_i$ = 90°. Although not documented directly in this report, other targets of interest to CEH applications that are not characterized by rotational symmetry as the landmines display similar patterns in terms of the maximum TCR bistatic scattering directions, which consistently correspond to the regions of low clutter return regardless of the target signature.

4. Analysis of Near-Field Bistatic Radar Images

In the remaining sections of this report we consider direct models of images of CEH targets obtained with the bistatic radar system based on simulations with the AFDTD software. Two types of sensing configurations are investigated in this context: near- and far-field geometries, each requiring different modes of the AFDTD code, imaging algorithms, and analysis tools. The near-field geometry represents a sensing scenario where both the radar Tx and Rx are relatively close to the target area: the Tx is fixed and the Rx consists of a linear antenna array with a fixed aperture length. In this case, the integration angle for the scattered signals is relatively small, approximately 20°. This sensing geometry would be typical for radar systems mounted on close-to-ground platforms, such as vehicles or small unmanned aerial vehicles (sUAVs). When the radar platform height is small (only a few meters), the range to target must be limited as well to keep the grazing angle above a certain floor (about 10°). The reason for this requirement is the well-known reduction in the target signature for close-to-ground radar systems due to the cancellation between the waves propagating along the direct and reflected radar-target paths.[7]

For the far-field geometry, both the Tx and Rx are placed at very large range from the target area: the Tx is fixed while the Rx describes a circular synthetic aperture with a wide integration angle (60°). This sensing geometry would be typical for long-range airborne radar systems flying on platforms high above the ground. Achieving large integration angles in this type of configuration is possible only by employing SAR techniques. Note that in this study we are not particularly concerned with the practical implementation of any of these bistatic radar systems, but rather with understanding the phenomenology and expected performance of such systems.

In the near-field models analyzed in this section, we consider that both the Tx and the Rx arrays are placed at 5 m horizontal range from the target and 2 m above the ground plane. The Rx array is 2 m wide and has 16 elements spaced 13.3 cm apart. We rotate this array in five different positions corresponding to the following azimuth bistatic angles (measured from the center of the array): 0°, 45°, 90°, 135° and 180°, while the height remains the same. The radar signal covers the 0.5- to 2-GHz frequency range in 51 steps with 30-MHz spacing between them. The Tx and Rx antennas are modeled as infinitesimal dipoles, oriented either vertically or horizontally (for horizontal polarization, the dipole is always oriented perpendicular to the Tx/Rx LOS).

Figure 28 provides a visual help in defining the downrange and cross-range directions, as well as the image resolution cell, for bistatic radar geometries. Thus, the constant-range ("isorange") curves in the image plane are ellipses with the Tx and Rx placed in their foci.[4] The downrange is the direction along the bisector of the bistatic angle, while the cross-range is the direction perpendicular to this bisector. The image resolution cell is a sector bordered by two constant-range ellipses, as shown in Fig. 28.

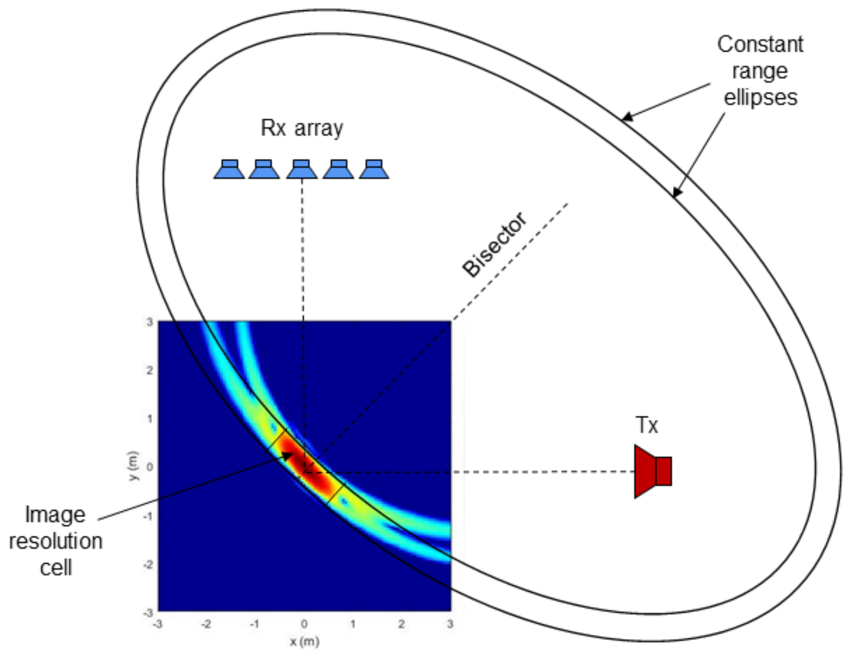

Fig. 28 Example of a near-field bistatic radar image, showing the main geometric elements characterizing the image resolution cell

We first analyze the PSF of the imaging system for various bistatic geometries by moving the Rx array around a circle at the azimuth angles listed in a previous paragraph. The point target is placed at the coordinate system origin (zero height) and its response is given by Eq. 4. The resulting images are shown in Fig. 29. Half of these images are obtained without any windowing of the Rx aperture, whereas for the other half we applied a Hanning tapering window across the Rx elements. In all cases we used a Hanning window in the frequency dimension of the data. As expected, the aperture tapering suppresses the cross-range sidelobes but at the same time degrades the cross-range resolution. Note the peculiar shape of the sidelobes in the images obtained for $\phi_s - \phi_i$ = 135° and 180°. In all near-field cases the sidelobes describe closed curves; however, these curves are clearly distinct from the isorange curves displayed in Fig. 28.

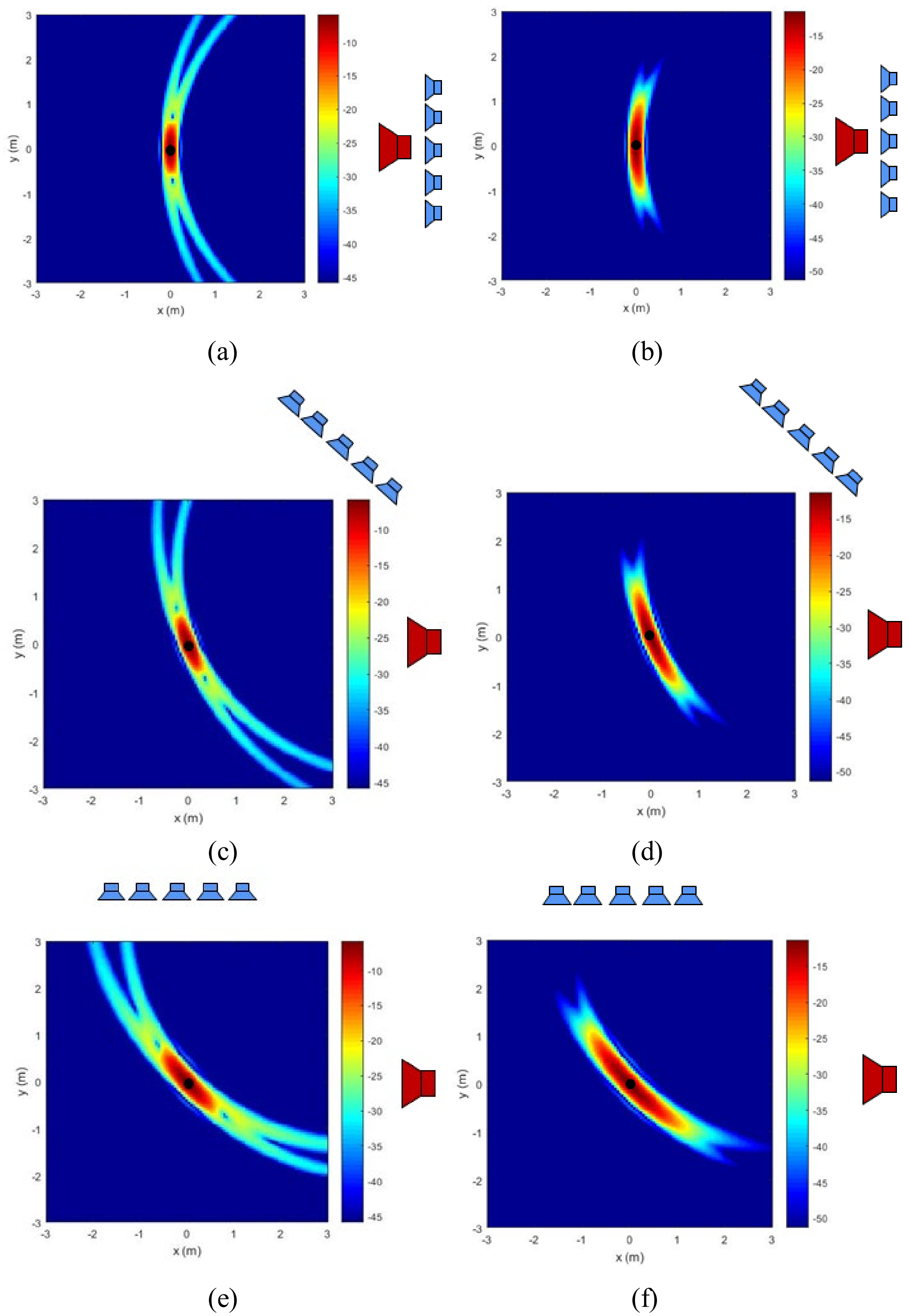

Fig. 29 PSF of the near-field bistatic radar system obtained for the following $\phi_s - \phi_i$ angles: a) 0°, no window; b) 0°, with window; c) 45°, no window; d) 45°, with window; e) 90°, no window; and f) 90°, with window. The black dot represents the point target location.

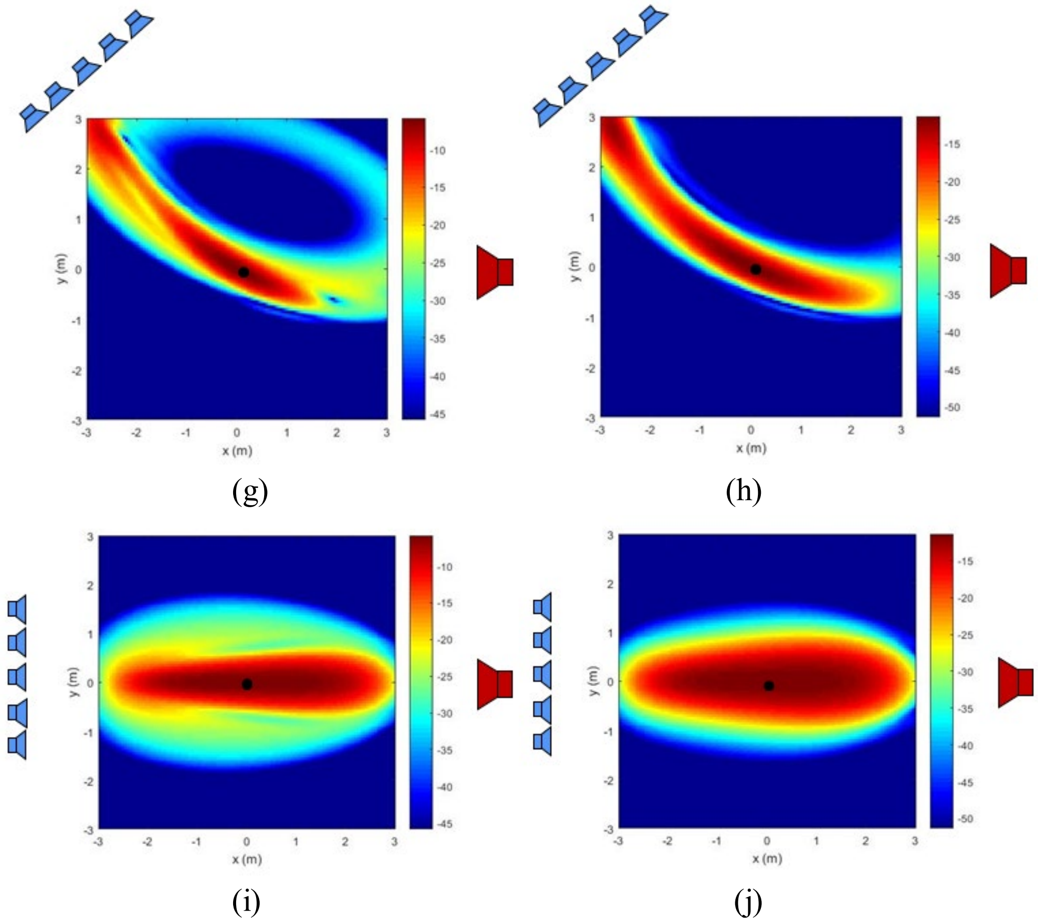

Fig. 29 PSF of the near-field bistatic radar system obtained for the following $\phi_s - \phi_i$ angles: a) 0°, no window; b) 0°, with window; c) 45°, no window; d) 45°, with window; e) 90°, no window; and f) 90°, with window. The black dot represents the point target location. (continued)

The most important lesson drawn from the images in Fig. 29 is the resolution degradation as the bistatic angle increases. The case where $\phi_s - \phi_i$ = 0°, which we call the "quasi-monostatic" geometry (although technically it is still bistatic), offers the best image resolution: 16 cm in downrange and 60 cm in cross-range. For $\phi_s - \phi_i$ = 45° or 90°, the resolution cell size increases slightly, but is still comparable to the monostatic case. However, as the bistatic angle exceeds 90° (as in $\phi_s - \phi_i$ = 135° or 180°), the degradation in image resolution is very rapid, with the resolution cell covering several meters in both directions. Importantly, the images representing the PSF are based strictly on the radar signal scattered by the target and do not include either the direct Tx–Rx propagation channel or the specular reflection from the ground.

Further analysis of the near-field images for the bistatic radar system is performed using AFDTD simulations of scattering by an M15 metallic landmine. The results are shown in Figs. 30–35. The target and its placement in the soil environment were described in Section 3.1, while the radar parameters were described in a previous paragraph of this section. For this sensing scenario, we consider both the V-V and H-H polarizations as well as one of the cross-polarization combinations. Additionally, we take advantage of the AFDTD software's ability to simulate either the signals scattered by the target alone or include the ground bounce with the target response in the radar received signal. As far as the direct signal propagating between Tx and Rx, this does not focus properly in the ground plane of the radar image, since both Tx and Rx are placed 2 m above the ground. Although a small residual of this signal can be noticed in some of the M15 bistatic radar images, this is not significant enough to alter our phenomenological conclusions. No Rx aperture tapering is performed in any of the images in Figs. 30–35.

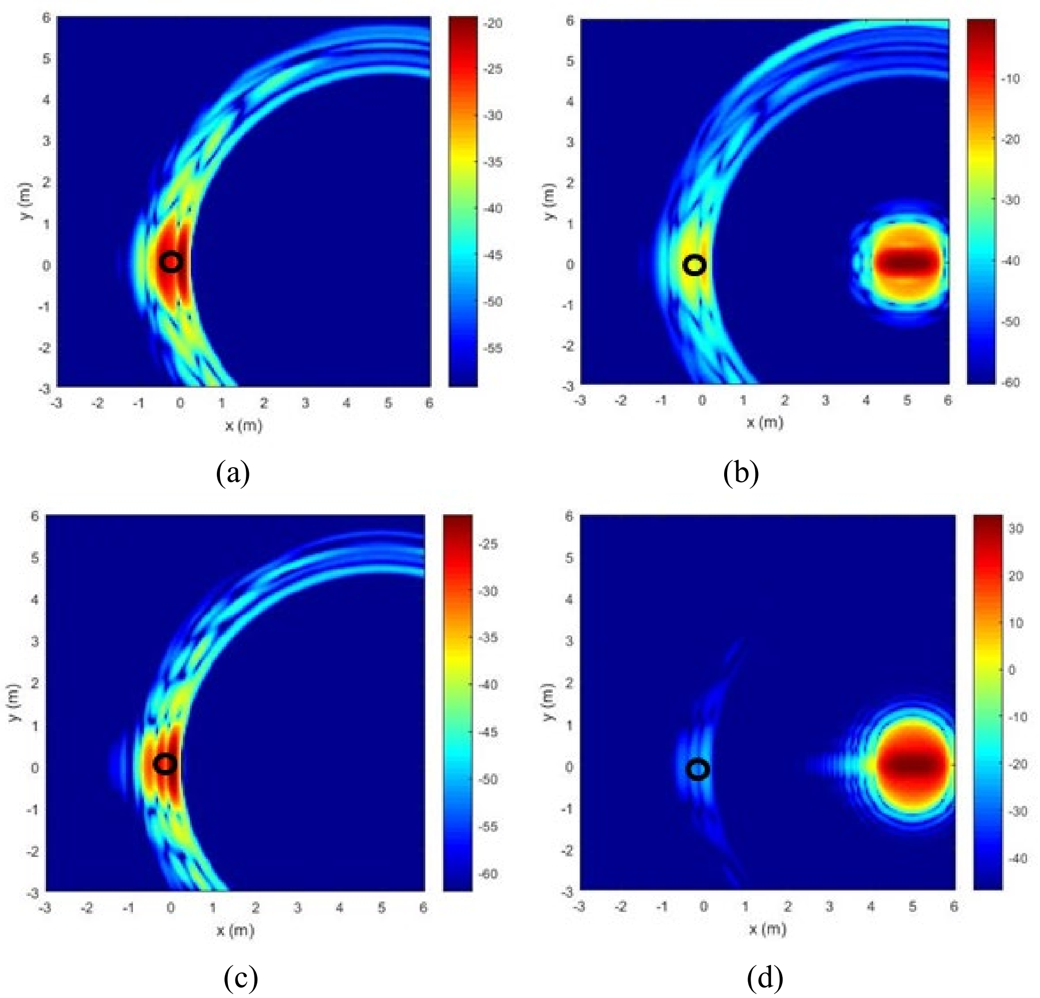

Fig. 30 Near-field bistatic radar images of an M15 landmine obtained for $\phi_s - \phi_i = 0°$; a) V-V polarization, no ground bounce; b) V-V polarization, with ground bounce; c) H-H polarization, no ground bounce; and d) H-H polarization, with ground bounce

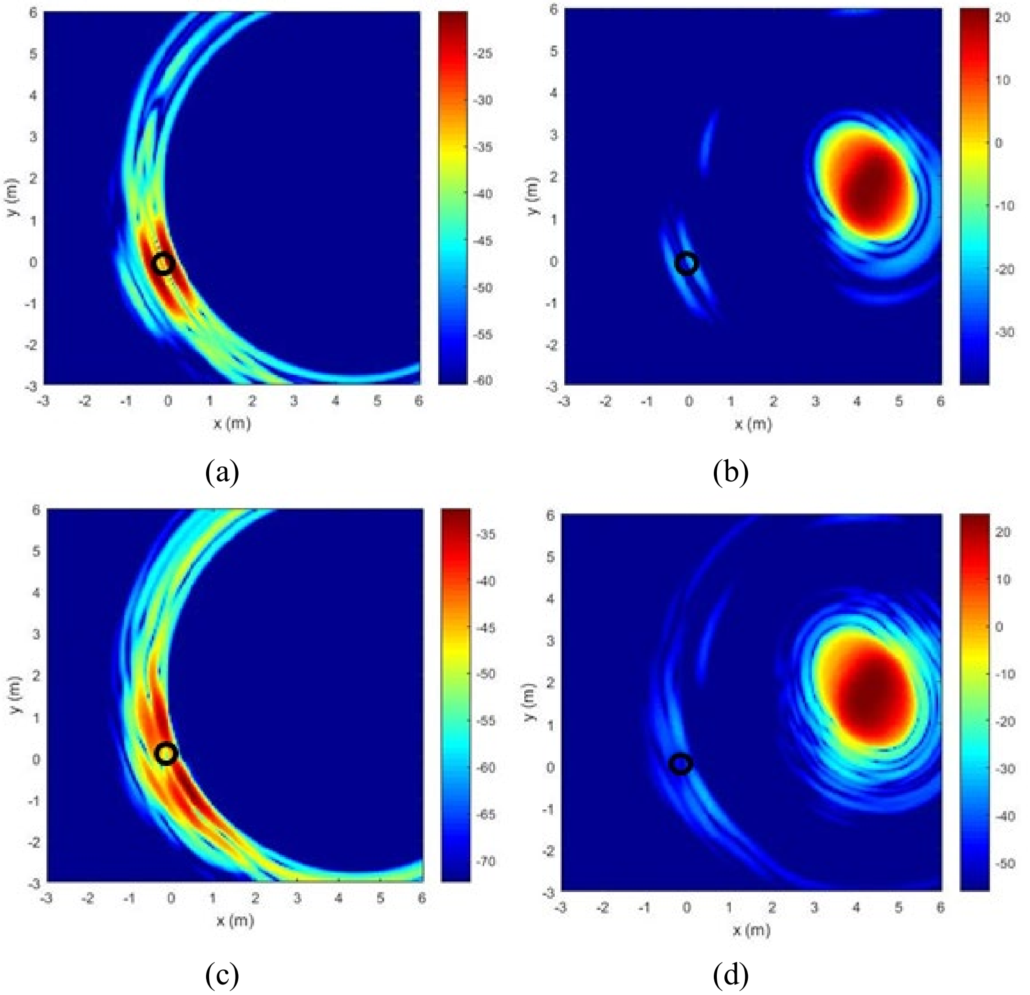

Fig. 31 Near-field bistatic radar images of an M15 landmine obtained for $\phi_s - \phi_i = 45°$; a) V-V polarization, no ground bounce; b) V-V polarization, with ground bounce; c) H-H polarization, no ground bounce; and d) H-H polarization, with ground bounce

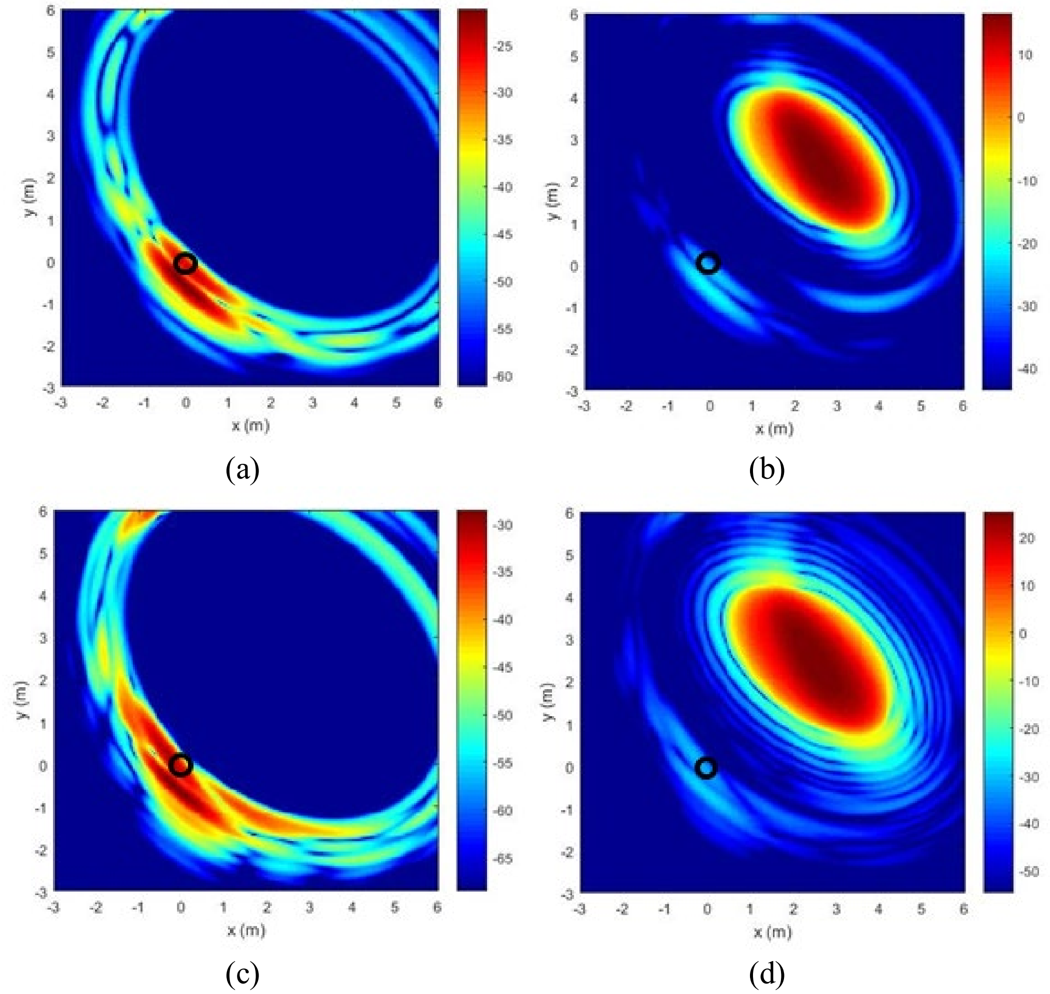

Fig. 32 Near-field bistatic radar images of an M15 landmine obtained for $\phi_s - \phi_i = 90°$; a) V-V polarization, no ground bounce; b) V-V polarization, with ground bounce; c) H-H polarization, no ground bounce; and d) H-H polarization, with ground bounce

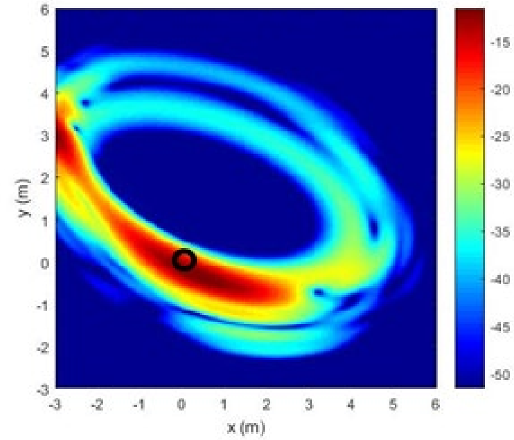

(a)

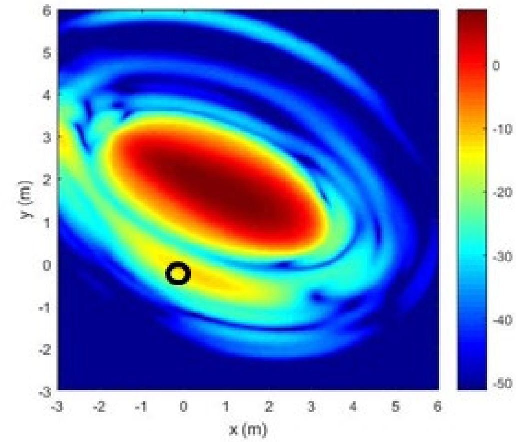

(b)

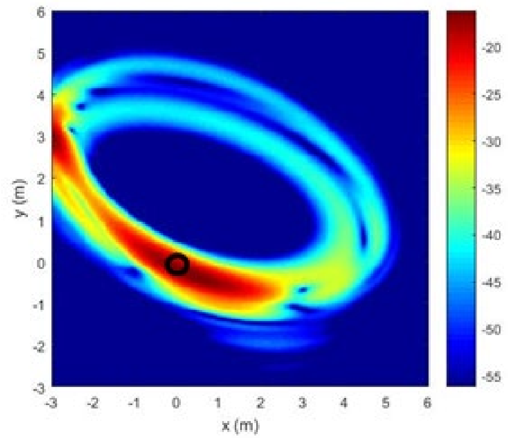

(c)

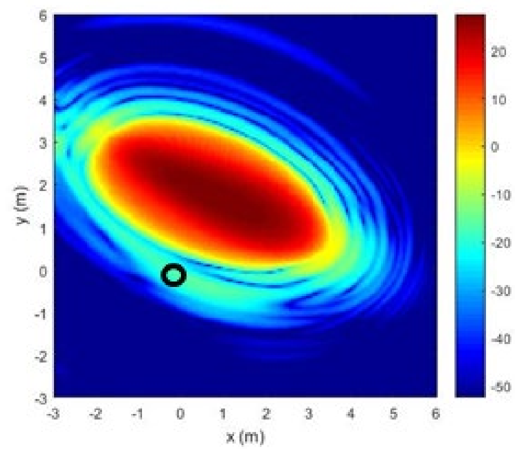

(d)

Fig. 33 Near-field bistatic radar images of an M15 landmine obtained for $\phi_s - \phi_i = 135°$; a) V-V polarization, no ground bounce; b) V-V polarization, with ground bounce; c) H-H polarization, no ground bounce; and d) H-H polarization, with ground bounce

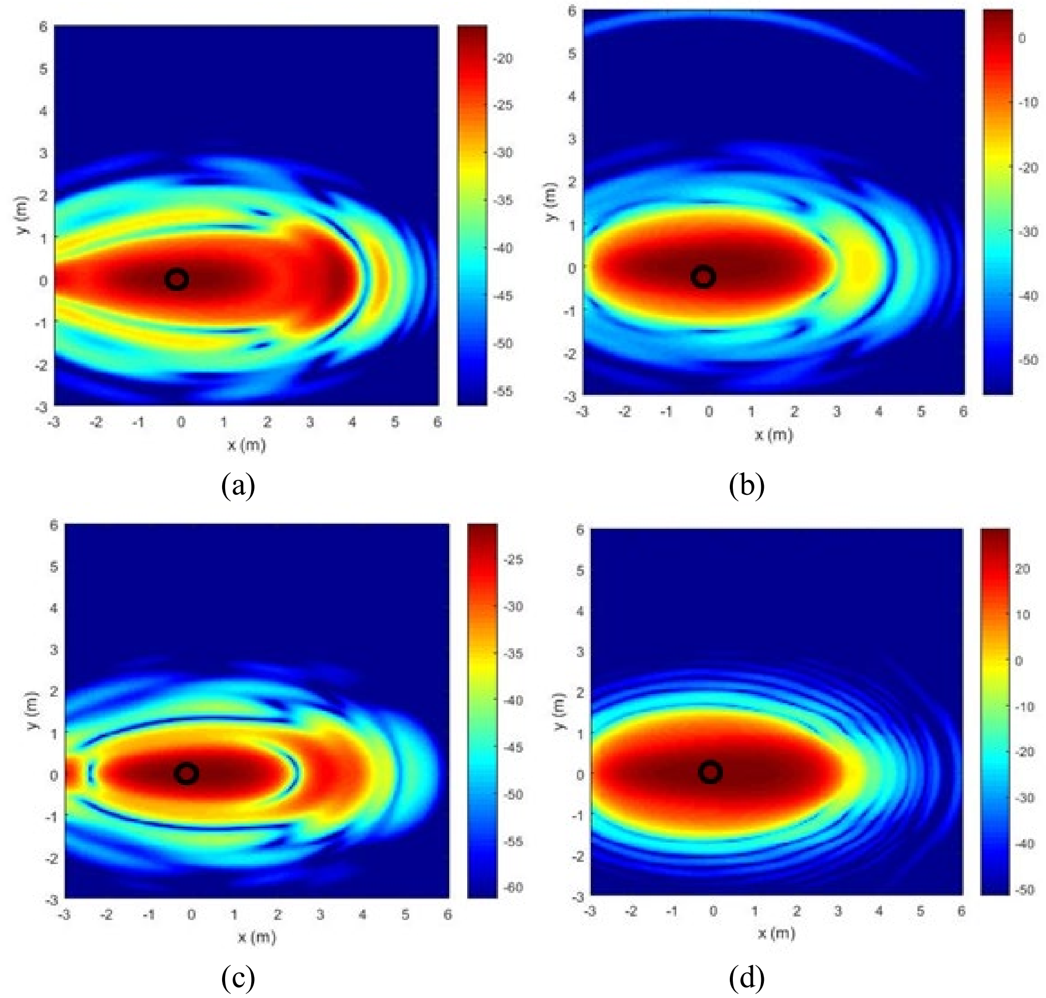

Fig. 34 Near-field bistatic radar images of an M15 landmine obtained for $\phi_s - \phi_i = 180°$; a) V-V polarization, no ground bounce; b) V-V polarization, with ground bounce; c) H-H polarization, no ground bounce; and d) H-H polarization, with ground bounce

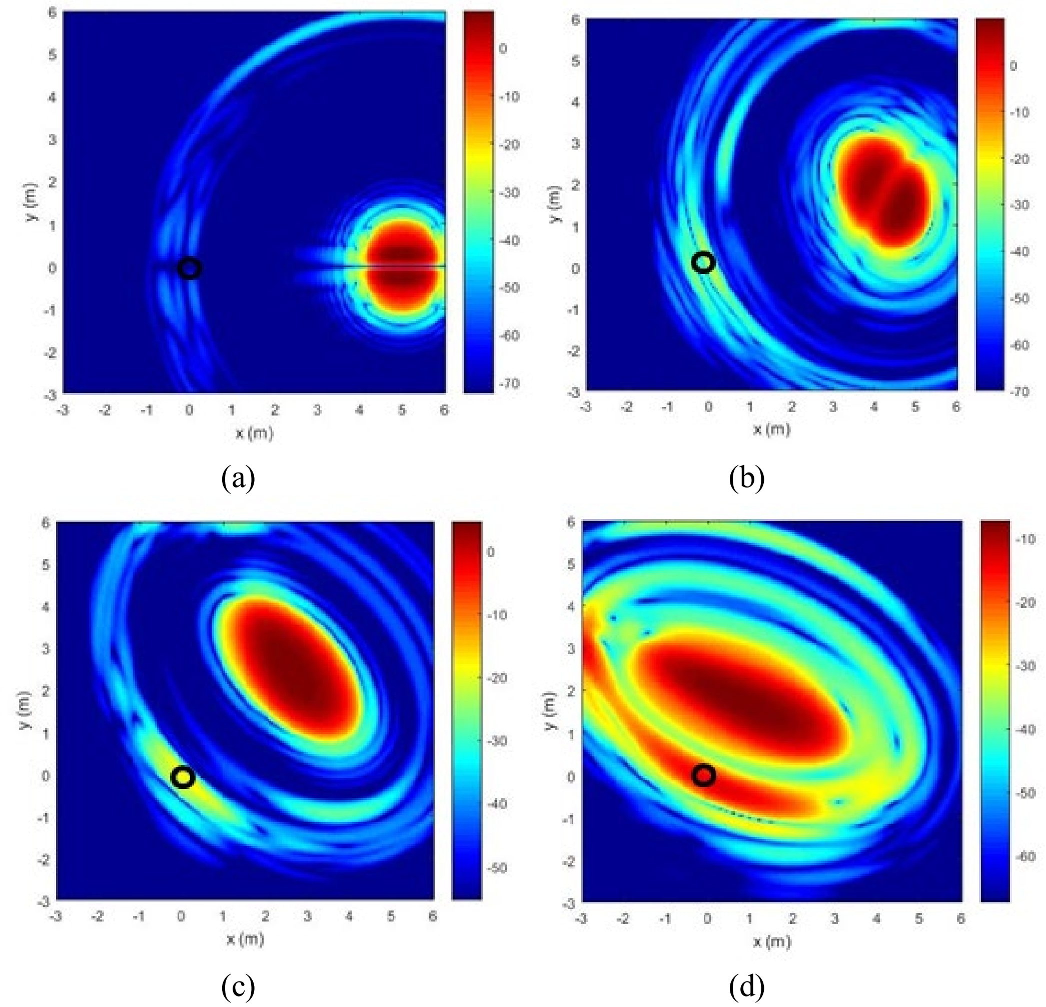

Fig. 35 Near-field bistatic radar images of an M15 landmine obtained for V-H polarization, with ground bounce and the following $\phi_s - \phi_i$ angles: a) 0°, b) 45°, c) 90°, and d) 135°

The M15 images that do not include the ground bounce tell a very similar story as the PSF images presented in Fig. 29. The main conclusion in this case is that the resolution degrades as the bistatic angle increases. However, the inclusion of the ground specular reflection in the radar images demonstrates new interesting effects characteristic to bistatic sensing geometries. Thus, the ground bounce appears in the radar image as a very bright spot orders of magnitude stronger than the target response. The two responses can be separated as long as the image resolution is good enough, as is the case for $\phi_s - \phi_i$ = 0°, 45° and 90°. However, for larger bistatic angles, the resolution is so poor that the target response becomes completely swamped by the ground bounce image.

Several additional comments regarding the images which include the ground bounce are needed at this point. First, the images which exclude this feature have only 40-dB dynamic range, whereas those including the ground bounce require higher dynamic range to distinguish the target signature at all (60 or 80 dB). Second, the ground bounce response is much stronger in H-H than in V-V polarization; consequently, the dynamic range is set to 60 dB for the V-V polarization images with ground bounce and to 80 dB for their H-H counterparts. Note that the image spot representing the ground bounce is not the antenna's beam footprint on the ground plane but rather the result of focusing this signal component in the radar image.

The cross-polarization images in Fig. 35 use the V-H combination (similar images were obtained for H-V) and always include the ground bounce signal. Note that this signal component still appears as a bright spot in these images, although its magnitude relative to the target response is generally smaller than in the co-polarization cases. (For the record, the images at $\phi_s - \phi_i$ = 0° and 45° use 80 dB dynamic range, while the images at $\phi_s - \phi_i$ = 90° and 135° use 60 dB dynamic range). However, the resolution degradation issue, and relatedly the separation between ground bounce and target response, remains the same regardless of polarization. Since very similar conclusions were drawn by simulating bistatic radar images of the TM62P2 plastic landmine, those results were omitted from this report.

One potential objection to the models presented in this section is that the small dipoles employed in the computer simulations do not represent realistic antennas for a practical radar system. In particular, dipoles have an almost omnidirectional pattern that creates strong coupling with the ground bounce for many possible bistatic sensing geometries. In practice, using directional antennas can partially mitigate this issue, as demonstrated, for instance, in the FLSAR systems,[1–3] where the specular ground bounce does not interfere with the radar image. However, this mitigation solution only works for backscatter geometries (β < 90°) and cannot suppress the specular ground bounce for forward geometries (β > 90°). Other ground-bounce suppression techniques based on signal processing (e.g., signal average subtraction[17]) can only achieve a limited improvement in the target-to-ground-bounce ratio, about 20 dB, which is likely insufficient to ensure detection of weak targets in bistatic radar images. Consequently, these images would necessitate very large dynamic ranges to accommodate both the target and the ground bounce responses; this in turn would put very stringent requirements on the radar system hardware.

For all the reasons discussed so far, we conclude that operating a bistatic radar imaging system for CEH application at large bistatic angles (β > 90°) is not recommended despite the potential improvement in TCR suggested in Section 3. Further evidence of the issues relevant to this sensing geometry is presented in Section 5, where we analyze far-field radar configurations.

5. Analysis of Far-Field Bistatic Radar Images

Although the near-field models of a bistatic radar imaging system presented in Section 4 are a relatively good representation of a possible practical implementation using a ground-based vehicle or sUAV platform, these models have certain limitations, primarily related to the AFDTD software capabilities. Thus, the near-field computer simulations cannot accommodate very large scenes, limiting the radar ranges to the target area. Additionally, we were not able to introduce rough terrain surfaces in the near-field models due to the high spatial sampling rates required.

To overcome these limitations, we performed a number of far-field models of the bistatic radar imaging system for CEH applications. As explained at the beginning of Section 4, these models represent a somewhat different sensing scenario compared with their near-field counterparts. However, with the far-field configurations, we were able to include rough ground surfaces, which allowed us to analyze the target images in the presence of terrain clutter. Moreover, these configurations lend themselves to an elegant *k*-space analysis of the imaging system resolution, which is not readily available for near-field geometries. One shortcoming of the far-field AFDTD models is that they cannot include the specular ground bounce in the radar received data; this signal component does not make physical sense in the context of excitation by a plane wave of infinite extent, as assumed by the far-field AFDTD models.

A comparison of the geometries of monostatic and a bistatic circular SAR systems operating in the far-field region, projected onto the horizontal plane x-y, is shown in Fig. 36. We assume that for the monostatic system both the Tx and Rx move along a circular trajectory, while for the bistatic system the Tx is fixed and the Rx moves on the same trajectory. A major question we try to answer in this section is how the image resolution varies with the sensing geometry (specifically, the bistatic angle) when the SAR system uses a constant integration angle (60°).

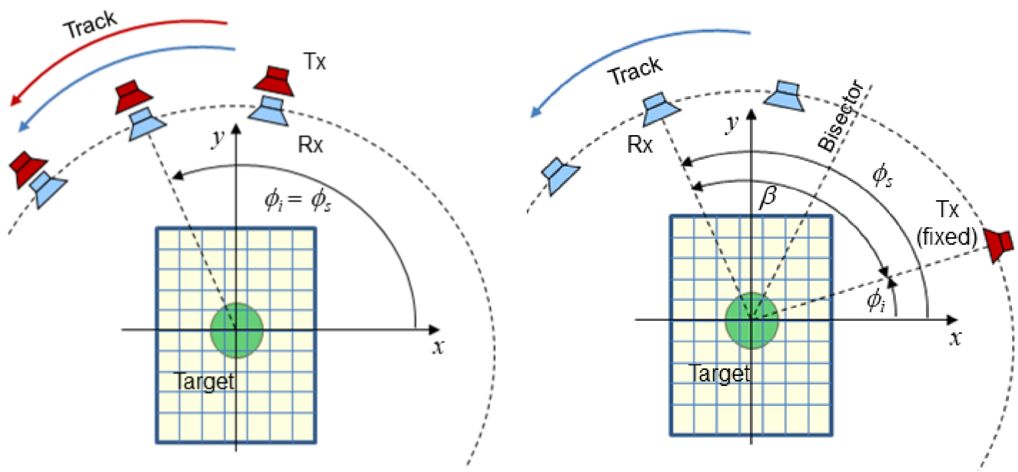

Fig. 36 Geometry of a generic spotlight SAR imaging system, showing a comparison of a) monostatic radar and b) bistatic radar

To perform this analysis, we adopt the tomographic view of SAR imaging systems.[18] In essence, this approach is based on the observation that the far-field radar measurements produce the spatial Fourier transform of the scene's reflectivity map; therefore, the reconstruction algorithm is equivalent to taking an inverse Fourier transform of the radar data. The Fourier counterpart of the spatial image domain is called the *k*-space, where each radar measurement represents a sample taken at the point $\mathbf{k}_s - \mathbf{k}_i$ in this space. Figure 37 represents the *k*-space support (restricted here to the k_x-k_y plane) of the SAR signal covering frequencies from f_1 to f_2 and azimuth angles from ϕ_1 to ϕ_2 for a monostatic and a bistatic system, respectively. In both cases the angle θ is the same for both Tx and Rx, meaning $\theta_i = \theta_s = \theta$, while the values of f_1, f_2, ϕ_1, and ϕ_2 are the same between the monostatic and bistatic SAR models.

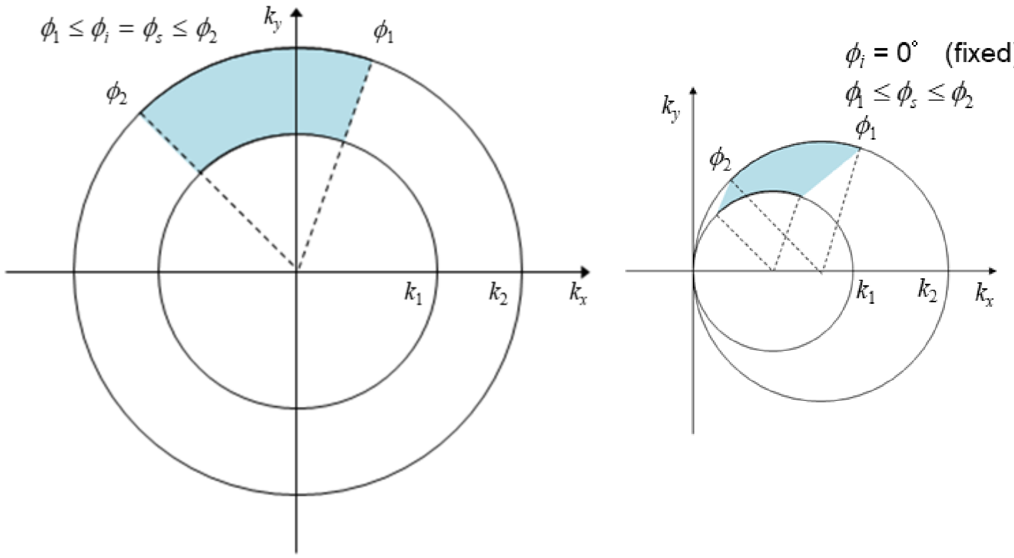

(a) (b)

Fig. 37 k-space representation of the radar signal support (shaded area) for a) monostatic SAR and b) bistatic SAR

In Fig. 37 we used the notations $k_1 = \frac{4\pi f_1}{c}\sin\theta$ and $k_2 = \frac{4\pi f_2}{c}\sin\theta$. The following formulas can be established:

$$\mathbf{k}_s - \mathbf{k}_i = 2k_0 \sin\theta \begin{bmatrix} \cos\phi_s \\ \sin\phi_s \end{bmatrix} \tag{10a}$$

for the monostatic radar system and

$$\mathbf{k}_s - \mathbf{k}_i = k_0 \sin\theta \begin{bmatrix} \cos\phi_s + 1 \\ \sin\phi_s \end{bmatrix} \tag{10b}$$

for the bistatic radar system, where $k_0 = \frac{2\pi f}{c}$. Using a well-known result in Fourier analysis, we infer that the larger the *k*-space support area of the radar data, the better the image resolution (smaller-resolution cell size). Figure 37 offers a clear intuitive explanation of the fact that the monostatic system (Fig. 37a) always provides better image resolution than the bistatic system (Fig. 37b), since the area covered in the *k*-space by the radar signals is larger (when f_1, f_2, ϕ_1, and ϕ_2 stay the same in both configurations). Furthermore, increasing the integration angle for the bistatic system does not always improve the resolution, unlike the situation encountered in the monostatic case. These statements are backed by quantitative results based on AFDTD simulations of the far-field radar sensing scenario.

Figure 38 displays the images of the buried M15 metallic landmine obtained by a far-field bistatic radar with synthetic Rx apertures centered at ϕ_s = 0°, 45°, 90°, 135°, and 180°. Other radar parameters are ϕ_i = 0°, $\theta_i = \theta_s$ = 65°, frequencies between 0.5 and 1.5 GHz in 51 steps, integration angle 60°, and V-V polarization. All the far-field images throughout this section use a sidelobe-control Hanning window in the angular domain. Next to each image in Fig. 38, we represented the corresponding radar signal support in the k_x-k_y plane. These diagrams clearly show the shrinkage of the support area as the bistatic angle increases and the consequent image-resolution degradation. Thus the case where the Rx aperture is centered at 0° (the "quasi-monostatic" case) offers the best resolution, comparable to that of a monostatic SAR. For small bistatic angles (β < 90°) the resolution loss is relatively small. However, for larger bistatic angles (β > 90°) the resolution loss is rapid; for instance, when β = 150°, the resolution cell stretches out four times in both dimensions compared with monostatic radar. As in the near-field case, the worst image resolution is obtained for the forward-scatter geometry, when ϕ_s = 180°.

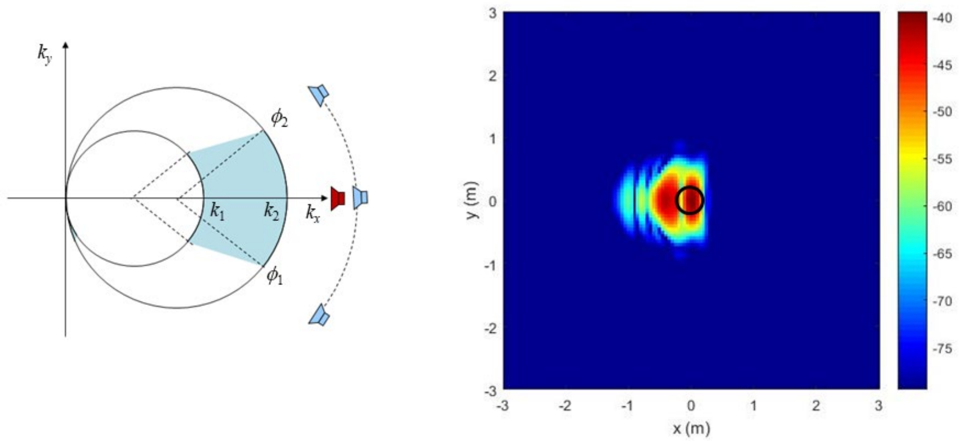

(a)

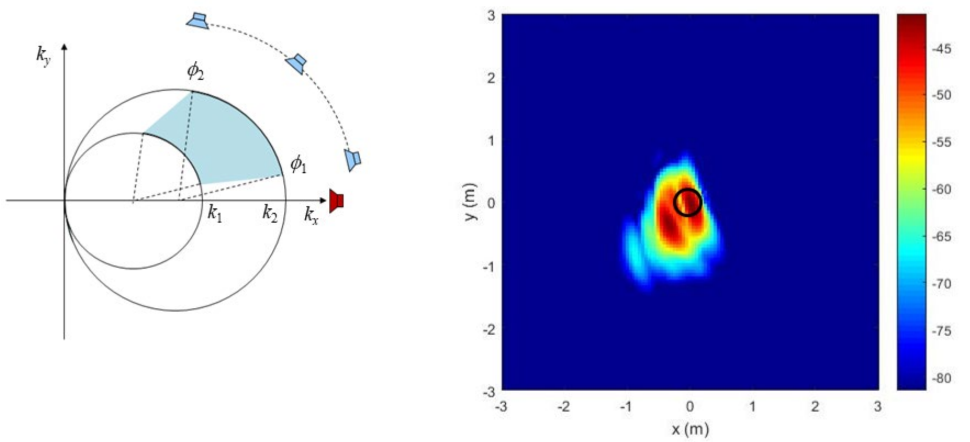

(b)

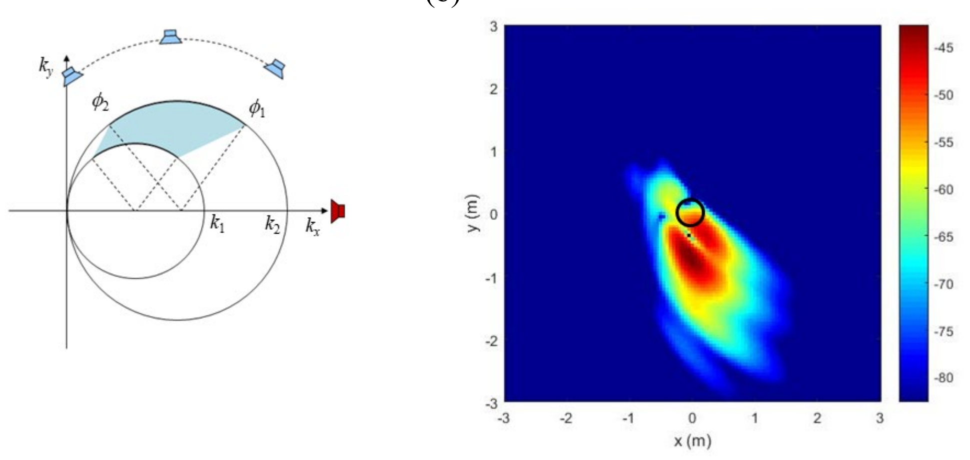

(c)

Fig. 38 Far-field bistatic radar images of an M15 landmine and their corresponding k-space diagrams, obtained for $\phi_i = 0°$ and $\theta_i = \theta_s = 65°$ and receiver apertures centered at ϕ_s equal to a) 0°, b) 45°, and c) 90°

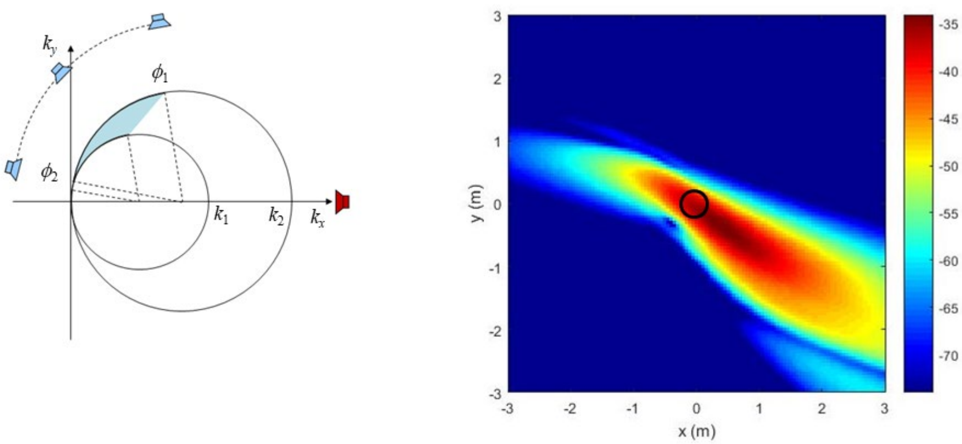

(d)

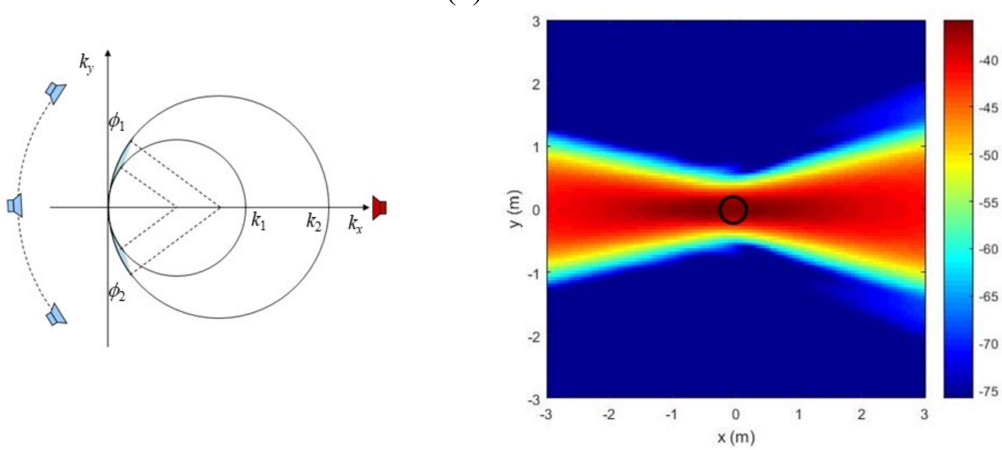

(e)

Fig. 38 Far-field bistatic radar images of an M15 landmine and their corresponding k-space diagrams, obtained for ϕ_i = 0° and θ_i = θ_s = 65° and receiver apertures centered at ϕ_s equal to d) 135° and e) 180° (continued)

It is also interesting to examine the scenario where the Tx and Rx are placed at different elevations ($\theta_i \neq \theta_s$). We assume that $\theta_i > \theta_s$, and let $\rho = \dfrac{\sin\theta_s}{\sin\theta_i} < 1$ (note that the case $\theta_i < \theta_s$ is somewhat similar and was omitted from this discussion). Then we have

$$\mathbf{k}_s - \mathbf{k}_i = k_0 \sin\theta_i \begin{bmatrix} \rho\cos\phi_s + 1 \\ \rho\sin\phi_s \end{bmatrix}, \tag{11}$$

and we obtain the *k*-space diagrams and images in Fig. 39 (for the same target and other radar parameters as in the previous simulations). In these figures, we denoted $k_{01} = \dfrac{4\pi f_1}{c}\sin\theta_i$ and $k_{02} = \dfrac{4\pi f_2}{c}\sin\theta_i$, where θ_i = 65°, θ_s = 45°. The images are very similar and show the same trend as those in Fig. 38. Interestingly, we notice that the image obtained in forward-scatter (ϕ_s = 180°), shown in Fig. 39e, displays somewhat better resolution than the image in Fig. 38e, due to wider support in the k-space when $\theta_i \neq \theta_s$; nevertheless, this resolution is still very poor compared with the small bistatic angle cases.

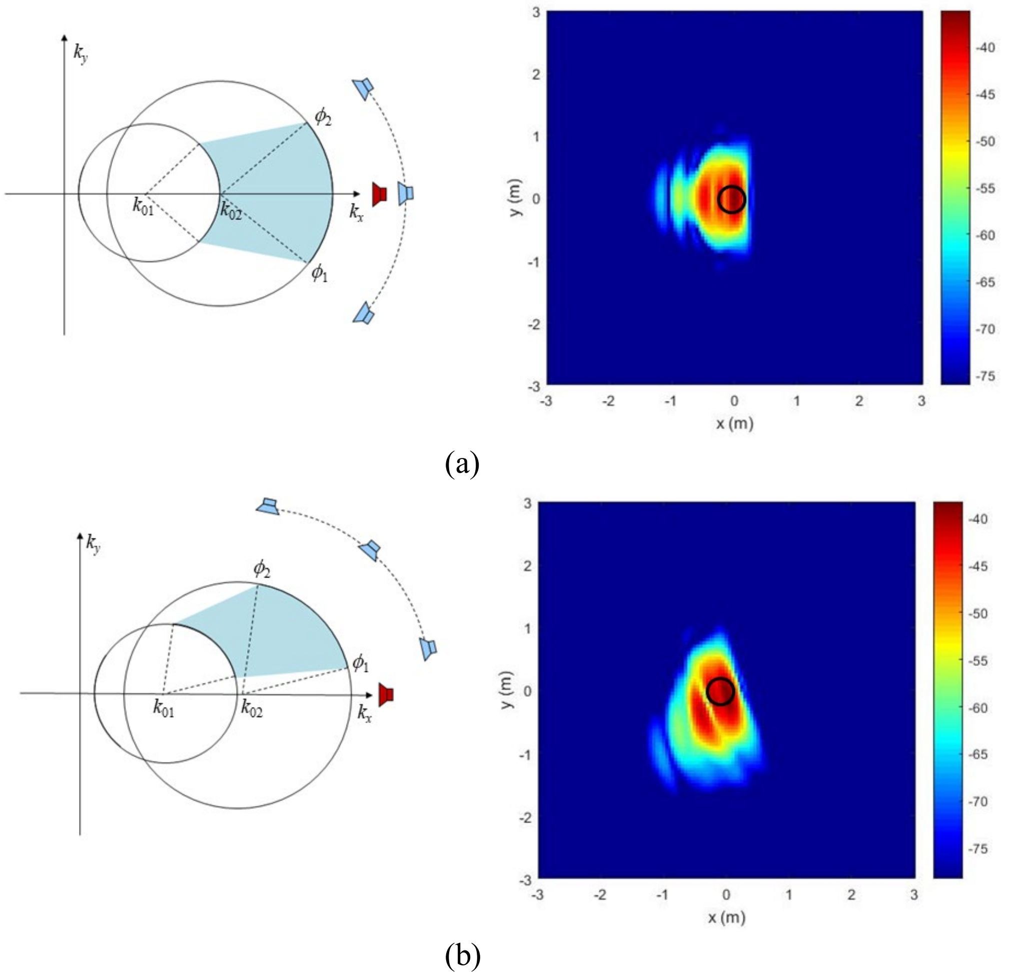

Fig. 39 Far-field bistatic radar images of an M15 landmine and their corresponding k-space diagrams, obtained for ϕ_i = 0°, θ_i = 65°, and θ_s = 45° and receiver apertures centered at ϕ_s equal to a) 0° and b) 45°

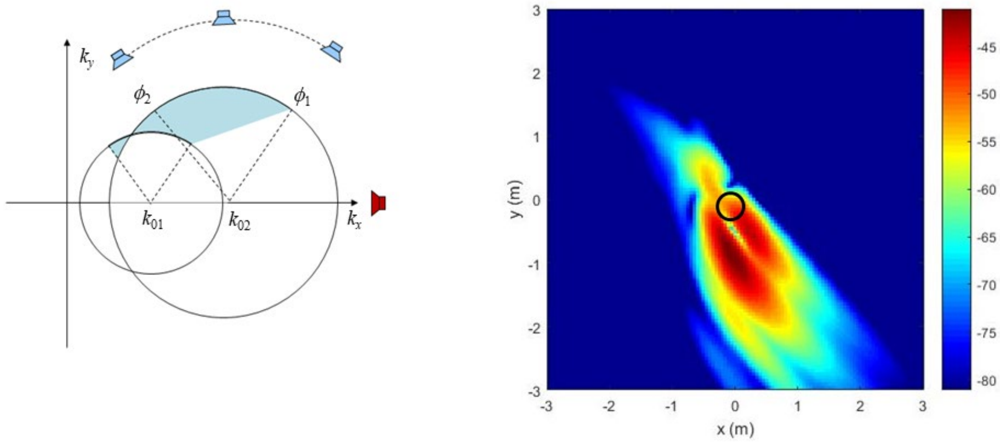

(c)

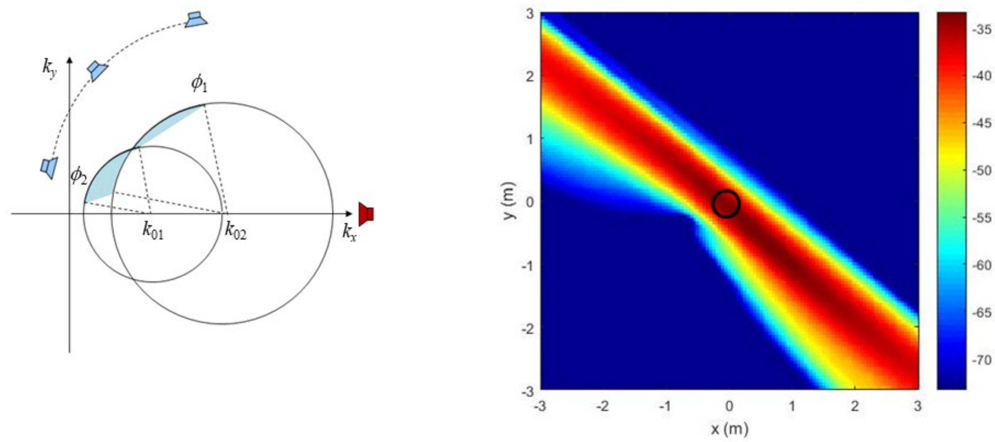

(d)

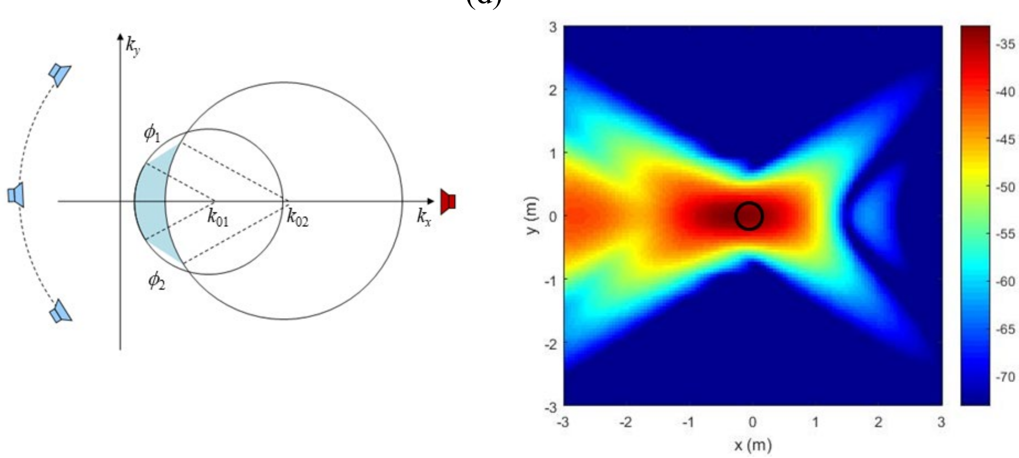

(e)

Fig. 39 Far-field bistatic radar images of an M15 landmine and their corresponding k-space diagrams, obtained for $\phi_i = 0°$, $\theta_i = 65°$, and $\theta_s = 45°$ and receiver apertures centered at ϕ_s equal to c) 90°, d) 135° and e) 180° (continued)

The next set of simulations consider the M15 metallic landmine buried under a random rough ground surface. The surface statistical parameters are the same as those used in Section 3.2 (h = 3 mm and L = 5 cm, with exponential correlation function) and we use the same radar parameters as in the simulations for Fig. 38 (equal Tx and Rx heights, with θ_i = θ_s = 65°). In Fig. 40 we consider the V-V and H-H polarization, while in Fig. 41 we show the images for V-H polarization. As in the previous far-field images, we move the center of the aperture to ϕ_s = 0°, 45°, 90°, 135°, and 180°. Note that the images contain only the incoherent component of the clutter generated by the ground surface. The blank (blue-colored) margin visible at the edges of some images in Fig. 40 is due to the fact that we simulated a rough surface patch of finite extent with an area smaller than the image itself.

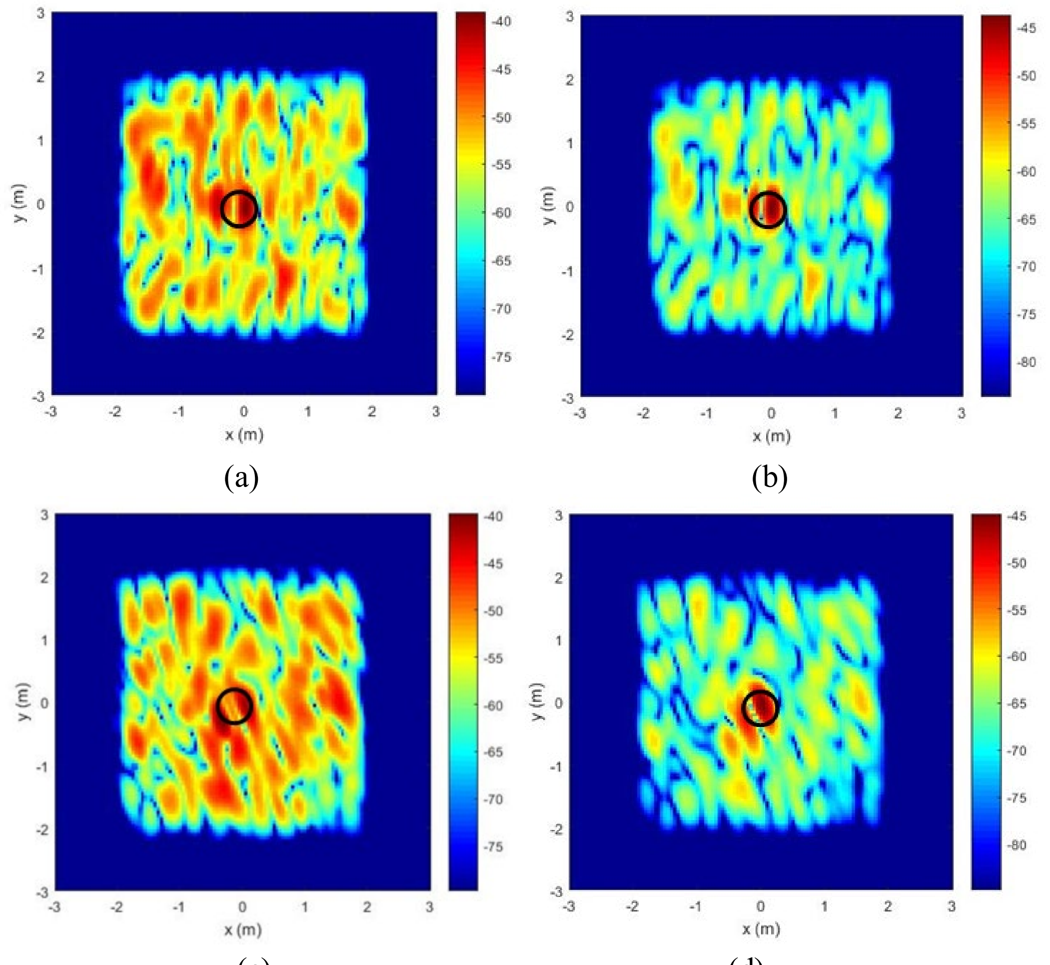

Fig. 40 Far-field bistatic radar images of an M15 landmine in the presence of rough surface clutter, obtained for receiver apertures centered at ϕ_s equal to a) 0°, V-V polarization; b) 0°, H-H polarization; c) 45°, V-V polarization; and d) 45°, H-H polarization

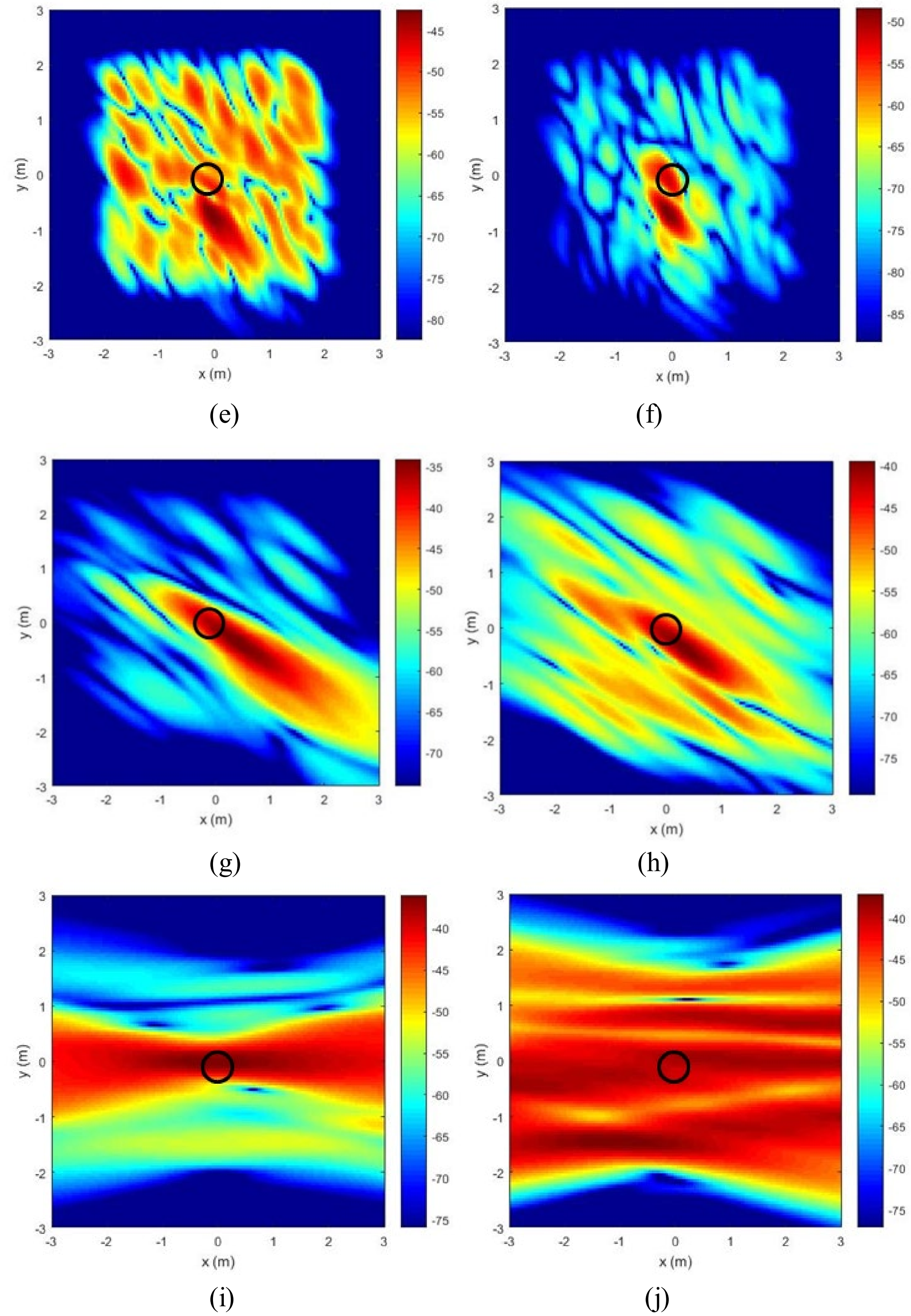

Fig. 40 Far-field bistatic radar images of an M15 landmine in the presence of rough surface clutter, obtained for receiver apertures centered at ϕ_s equal to e) 90°, V-V polarization; f) 90°, H-H polarization; g) 135°, V-V polarization; h) 135°, H-H polarization; i) 180°, V-V polarization; and j) 180°, H-H polarization (continued)

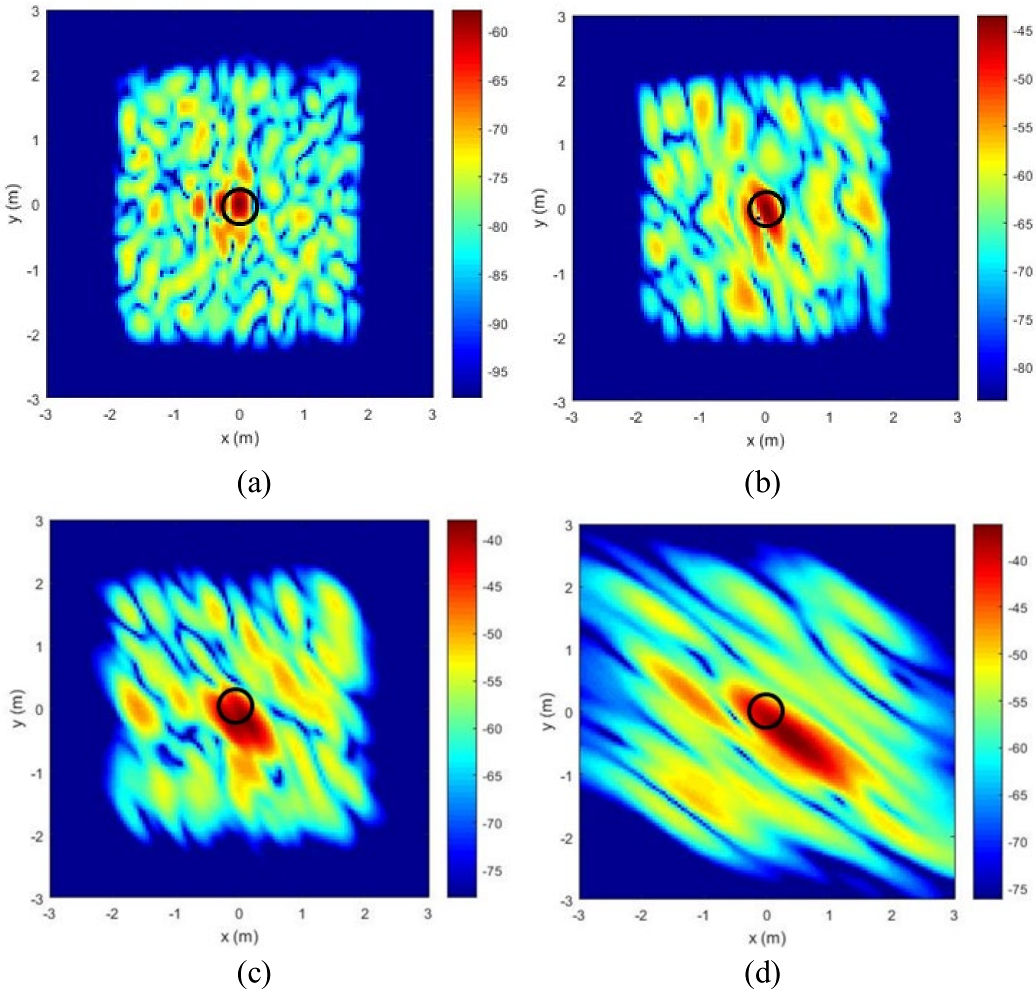

(a) (b) (c) (d)

Fig. 41 Far-field bistatic radar images of an M15 landmine in the presence of rough surface clutter, obtained for V-H polarization and receiver apertures centered at ϕ_s equal to a) 0°, b) 45°, c) 90° and d) 135°

This time we investigate the impact of the change in resolution with the bistatic angle on the TCR. To compute the image TCR, we take the magnitude ratio between the largest image pixel and the average of the remaining pixels covering the rough ground area. The numerical values of this performance metric are summarized in Table 3 for the three polarization combinations.

Table 3 TCR values in dB, computed directly from the bistatic radar images of the M15 and TM62P2 landmines in terrain clutter for various polarizations and bistatic angles

Bistatic angle	M15			TM62P2	
	V-V	H-H	V-H	V-V	H-H
0°	14	21	21	4	10
45°	12	21	19	3	9
90°	13	26	20	0	10
135°	27	17	19	7	1
180°	22	12	…	3	0

Analyzing the results in Table 3, we notice that the H-H polarization offers better TCR than V-V for small bistatic angles ($\beta < 90°$), where the image resolution is satisfactory. However, $\beta = 135°$ displays very large TCR for V-V polarization, which was expected from the results in Section 3.2. Nonetheless, the image resolution in Fig. 40g is very poor, meaning that this sensing geometry is not a good solution for detecting the buried target. Interestingly, the V-H cross-polarization combination provides TCR values comparable to the H-H case, which again was predicted by the models in Section 3.2. Relating the TCR results from Table 2 to those in Table 3, the models in Section 3.2 used an integration angle of about 6° compared with 60° for the models in the current section. Therefore, the SAR images in Figs. 40 and 41 should theoretically produce TCR numbers that are 10 dB higher than the ones in Table 2. The fact that this difference is not achieved in practice suggests that the larger integration angle does not provide the TCR improvement predicted by the theory and simple model in Section 3.2.

All the results presented in this section reinforce the previous conclusions that operating the bistatic imaging radar at large bistatic angles ($\beta > 90°$) is not a good sensing configuration for CEH applications. Note that the far-field images obtained for the TM62P2 plastic landmines were omitted again due to the lack of space. However, those images do not reveal any new phenomenology that was not already present in the images shown in this section. In fact, since the plastic landmine's radar signature is very weak, detection of that target in the presence of terrain clutter is problematic even for monostatic (or small bistatic angle) configurations.[19]

6. Simulation of an FLSAR System in Monostatic and Bistatic Configurations

In this section we consider a more complex simulation scenario, where an FLSAR system is configured either in a quasi-monostatic or a forward-scatter bistatic geometry. The operational principle of the quasi-monostatic FLSAR system modeled here is similar to that of the SIRE and SAFIRE radar systems, although the parameters (particularly, the forward aperture integration lengths) are different. The bistatic radar system is entirely fictitious and does not correspond to any existing implementation. The two configurations and their sensing geometries are shown in Fig. 42. Those figures include two scattering objects: a shallow-buried M15 metallic landmine and a rock of similar dimensions placed on the ground surface. The model considered a flat ground, which means the rough terrain clutter was ignored.

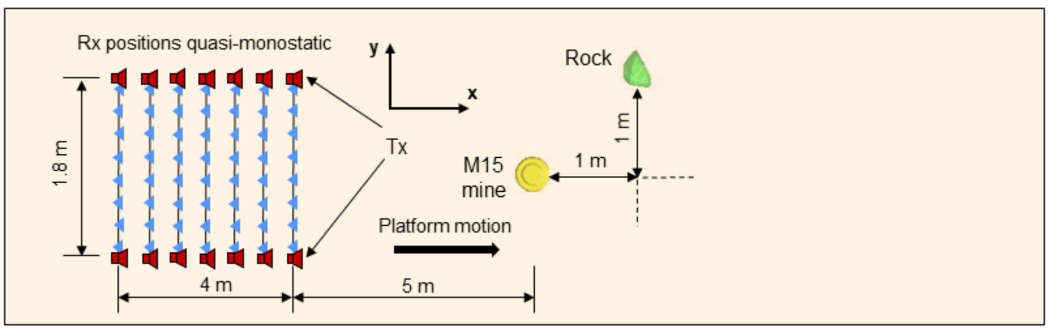

(a)

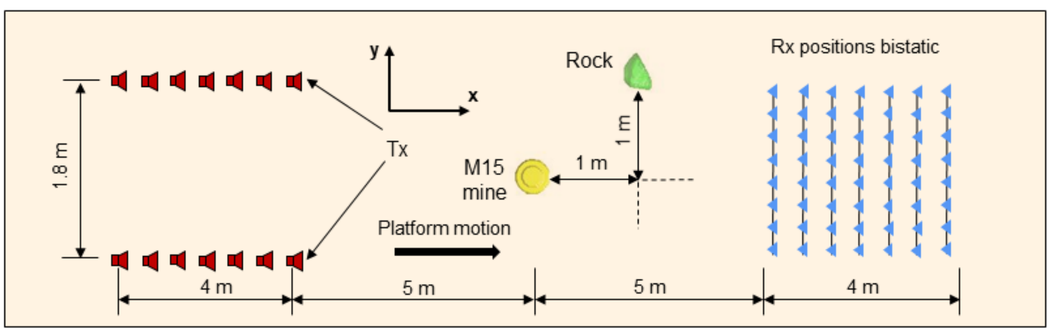

(b)

Fig. 42 Geometry of the FLSAR system modeled in Section 6, configured to operate in a) quasi-monostatic mode and b) bistatic mode

The radar system involves two Tx separated by 1.8 m in the y direction and an array of 16 equally spaced Rx elements, forming a 1.8-m-wide physical aperture. In both configurations, the Tx and Rx elements move in lockstep in the x direction and we take radar measurements at 11 successive positions along the x axis, with 0.4-m spacing between them. At every position along x, each Tx transmits separately, while the 16 Rx elements record the scene's scattering return simultaneously. The antenna elements (both Tx and Rx) are infinitesimal dipoles with vertical orientation placed at 2 m above the ground. The radar frequency varies between 0.5 and 2 GHz in 151 steps spaced 10 MHz apart.

The difference between the quasi-monostatic and bistatic configurations consists of the relative positions between the two Tx's and the Rx array. In the first case, they are all on the same side of the target area (in backscatter), whereas in the second case, they are on opposite sides of the target area (in forward-scatter). The image area extends ±4 m in the x direction from the origin (which coincides with the M15 location). All the radar data recorded during the Tx–Rx activation sequence described in the previous paragraph are used in creating every image pixel according to Eq. 2.

The results are shown in Fig. 43, where we represented the images obtained with and without the ground bounce for the two separate configurations. Note that the rock has a much larger signature than the landmine since it is placed above the ground (versus buried). As a result, the imaging system's resolution is critical in being able to separate the target (the landmine) from the discrete clutter item (the rock). Additionally, unless we employ signal processing techniques capable of suppressing the ground bounce in the radar image, this phenomenon may strongly compete with and overrun the target return.

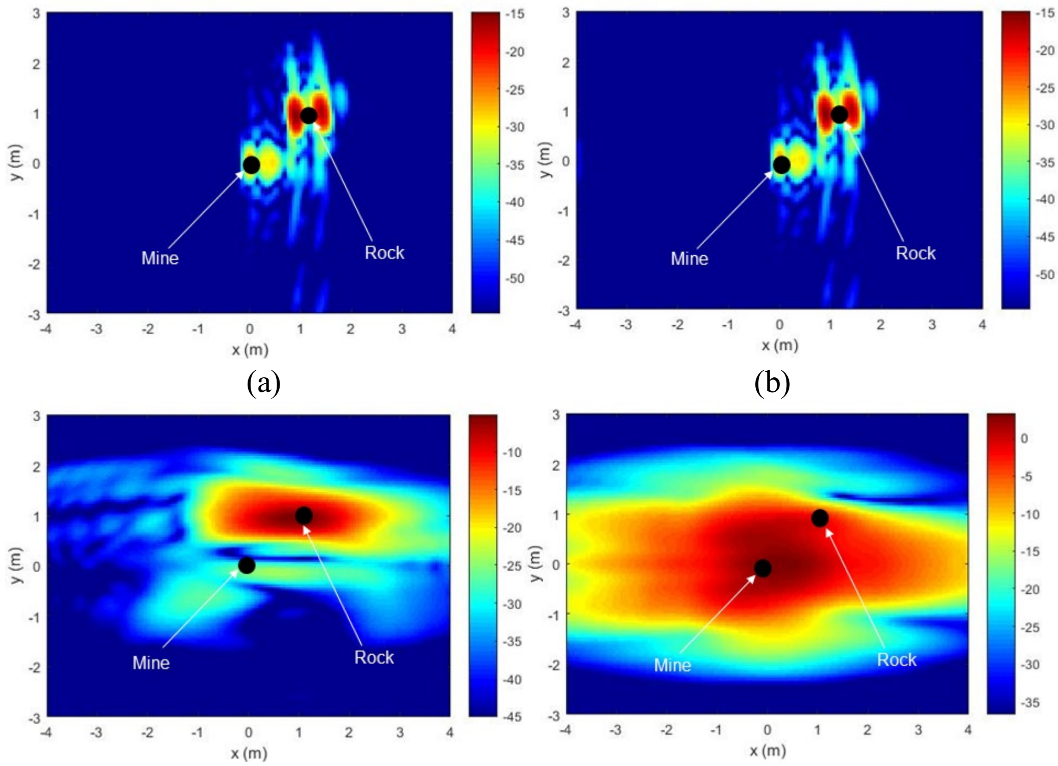

(a) (b) (c) (d)

Fig. 43 Images of the scene involving an M15 landmine and a rock, obtained with the FLSAR system for a) quasi-monostatic mode, without ground bounce; b) quasi-monostatic mode, with ground bounce; c) bistatic mode, without ground bounce; and d) bistatic mode, with ground bounce. The black dots represent the locations of the landmine and rock.

The images in Fig. 43 are very conclusive in demonstrating why the forward-scatter bistatic geometry is unfavorable for radar imaging of targets in CEH applications. Namely, there are two major problems with this configuration: 1) the loss of resolution makes it difficult to separate the target from discrete clutter items, and 2) the specular ground bounce occupies approximately the same image area as the target, with the signature of the former being much stronger than the latter. Notice that for the quasi-monostatic system the image resolution is fine enough to spatially separate the two objects in the scene (in fact, this geometry offers the best resolution achievable with these radar parameters), while the ground bounce is completely absent from the image area.

7. Conclusions

In this report we investigated the expected performance of active, coherent bistatic radar imaging systems for CEH applications. The study consisted of various numerical models of such hypothetical systems, using the frequency band and aperture configurations of existing imaging radar implementations.

The first part of our investigation was concerned with the target signature and the TCR in the presence of terrain clutter. The models showed that improved TCR can be achieved for certain bistatic geometries as compared with traditional monostatic radar. In particular, we found a low-clutter region characteristic to V-V polarization and corresponding to a bistatic angle of approximately 135°, where the TCR is maximized.

However, the analysis of radar images of CEH targets obtained with bistatic systems demonstrated the two major shortcomings of this sensing modality: 1) the image resolution degradation at large bistatic angles and 2) the difficulty in separating the target response from the specular ground bounce in the image. These issues were illustrated with multiple numerical examples, involving both near-field and far-field geometries. In particular, the far-field cases analyzed in Section 5 allowed a clear interpretation of the resolution loss issue by using the *k*-space representation of the radar signal support. Additionally, the models of a forward-looking-like radar imaging system in Section 6 offered solid evidence that a quasi-monostatic configuration (used by some existing FLSAR systems) provides superior performance compared with a hypothetical forward-scatter bistatic radar system.

One major consideration not discussed in this report is the practical difficulty in building the hardware of a bistatic radar system, especially when the Tx and Rx modules are installed on separate platforms. Thus achieving the time and phase synchronization between the two modules, required for coherent signal integration in a radar image, is much more challenging than in the traditional monostatic, single-platform radar systems. Some mitigation of the direct signal between Tx and Rx may also be necessary: Although this signal does not appear well-focused in the ground-plane radar image, its large magnitude can have negative effects on the Rx operation (for example, by saturating the Rx front-end amplifier).

The conclusion we draw from this study is that a bistatic imaging radar system involving large separation between Tx and Rx (large bistatic angles) is not a practical solution for CEH applications, since it provides inferior performance to existing quasi-monostatic FLSAR systems, while at the same time being much more difficult to build. Nevertheless, some of the bistatic radar concepts are still potentially useful in these applications. One obvious remark is that bistatic geometries characterized by small bistatic angles are actually used in many existing radar sensors (including the FLSAR systems mentioned in the Introduction). Another productive direction of investigation is offered by noncoherently combining the measurements from multiple separate receivers, either in the presence of active transmitters or using opportunistic RF signals in passive bistatic radar systems. These techniques are currently receiving a great deal of interest in the radar research community.[6]

8. References

1. Ton T, Wong D, Soumekh M. ALARIC forward-looking ground penetrating radar system with standoff capability. Proceedings of the IEEE International Conference on Wireless Information Technology and Systems; 2010; Honolulu, HI. www.proceedings.com/10020.html.
2. Ressler M, Nguyen L, Koenig F, Wong D, Smith G. The ARL synchronous impulse reconstruction (SIRE) forward-looking radar. Proceedings of SPIE. 2007 May;6561.
3. Phelan B, Ranney K, Gallagher K, Clark J, Sherbondy K, Narayanan R. Design of ultra-wideband (UWB) stepped-frequency radar (SFR) for imaging of obscured targets. IEEE Sensors Journal. 2017;17(14).
4. Willis N. Bistatic radar. Norwood (MA): Artech; 1991.
5. Skolnik M. Radar handbook. New York (NY): McGraw Hill; 2008.
6. Melvin W, Scheer J. Principles of modern radar – radar applications. Edison (NJ): SciTech Publishing; 2014.
7. Richards M, Scheer J, Holm W. Principles of modern radar – basic principles. Raleigh (NC): SciTech Publishing; 2010.
8. Dogaru T. AFDTD user's manual. Adelphi (MD): Army Research Laboratory (US); 2010 Mar. Report No.: ARL-TR-5145.
9. Dogaru T. NAFDTD – a near-field finite difference time domain solver. Adelphi (MD): Army Research Laboratory (US); 2012 Sep. Report No.: ARL-TR-6110.
10. Ruch, G, Barrick DE, Stuart WD, Krichbaum CK. Radar cross section handbook. New York (NY): Plenum Press; 1970.
11. Liao D, Dogaru T. Full-wave characterization of rough terrain surface scattering for forward-looking radar applications. IEEE Transactions on Antennas and Propagation. 2012;60(8):3853–3866.
12. Dogaru T, Liao D. Validating models of bistatic scattering from dielectric surfaces with small roughness. Proceedings of IEEE Symposium on Antennas and Propagation; 2018; Boston, MA.
13. Ulaby FT, Long DG. Microwave radar and radiometric remote sensing. Ann Arbor (MI): University of Michigan Press; 2014.

14. Tsang L, Kong JA. Scattering of electromagnetic waves – advanced topics. New York (NY): Wiley; 2001.

15. Johnson JT, Ouellette JD. Polarization features in bistatic scattering from rough surfaces. IEEE Transactions on Geoscience and Remote Sensing. 2014; 52(3): 1616-1626.

16. Soumekh M. Synthetic aperture radar signal processing. New York (NY): Wiley; 1999.

17. Nguyen L, Dogaru T, Innocenti R. Signal and image processing for underground target detection using the NIITEK ground penetrating radar (GPR). Adelphi (MD): Army Research Laboratory (US); 2009 Apr. Report No.: ARL-TR-4778.

18. Jakowatz C, Wahl D, Eichel P, Ghiglia D, Thompson P. Spotlight-mode synthetic aperture radar: a signal processing approach. Boston (MA): Kluwer Academic Publishers; 1996.

19. Dogaru T, Le C. Polarization differences in airborne ground penetrating radar performance for landmine detection. Proceedings of SPIE. 2016 May;9829.

List of Symbols, Abbreviations, and Acronyms

2-D	two-dimensional
3-D	three-dimensional
ARL	Army Research Laboratory
CCDC	Combat Capabilities Development Command
CEH	counter-explosive hazard
dB	decibels
dBsm	decibels-square-meter
EM	electromagnetic
FDTD	finite-difference time-domain
FLSAR	forward-looking synthetic aperture radar
H-H	horizontal–horizontal
H-V	horizontal–vertical
LOS	line of sight
PSF	point spread function
RCS	radar cross section
RF	radio frequency
Rx	receiver
SAFIRE	Spectrally Agile Frequency-Incrementing Reconfigurable
SAR	synthetic aperture radar
SIRE	Synchronous Impulse Reconstruction
SPM	small perturbation method
sUAV	small unmanned aerial vehicle
TCR	target-to-clutter ratio
Tx	transmitter
UWB	ultra-wideband

V-H	vertical–horizontal
V-V	vertical–vertical

1 (PDF)	DEFENSE TECHNICAL INFORMATION CTR DTIC OCA
1 (PDF)	CCDC ARL FCDD RLD CL TECH LIB
1 (PDF)	GOVT PRINTG OFC A MALHOTRA
6 (PDF)	CCDC ARL FCDD RLS RU A SULLIVAN T DOGARU C LE B PHELAN K SHERBONDY FCDD RLS RW K RANNEY